

THE *CHANDRA* LOCAL VOLUME SURVEY: THE X-RAY POINT SOURCE CATALOG OF NGC 300B. BINDER<sup>1</sup>, B. F. WILLIAMS<sup>1</sup>, M. ERACLEOUS<sup>2</sup>, T. J. GAETZ<sup>3</sup>, P. P. PLUCINSKY<sup>3</sup>, E. D. SKILLMAN<sup>4</sup>, J. J. DALCANTON<sup>1</sup>,  
S. F. ANDERSON<sup>1</sup>, D. R. WEISZ<sup>1</sup>, A. K. H. KONG<sup>5</sup>

Draft version August 16, 2012

## ABSTRACT

We present the source catalog of a new *Chandra* ACIS-I observation of NGC 300 obtained as part of the *Chandra* Local Volume Survey. Our 63 ks exposure covers  $\sim 88\%$  of the  $D_{25}$  isophote ( $R \approx 6.3$  kpc) and yields a catalog of 95 X-ray point sources detected at high significance to a limiting unabsorbed 0.35–8 keV luminosity of  $\sim 10^{36}$  erg s<sup>−1</sup>. Sources were cross-correlated with a previous *XMM-Newton* catalog, and we find 75 “X-ray transient candidate” sources that were detected by one observatory, but not the other. We derive an X-ray scale length of  $1.7 \pm 0.2$  kpc and a recent star formation rate of  $0.12 M_{\odot} \text{ yr}^{-1}$ , in excellent agreement with optical observations. Deep, multi-color imaging from the *Hubble Space Telescope*, covering  $\sim 32\%$  of our *Chandra* field, was used to search for optical counterparts to the X-ray sources, and we have developed a new source classification scheme to determine which sources are likely X-ray binaries, supernova remnants, and background AGN candidates. Finally, we present the X-ray luminosity functions (XLFs) at different X-ray energies, and we find the total NGC 300 X-ray point source population to be consistent with other late-type galaxies hosting young stellar populations ( $\lesssim 50$  Myr). We find XLF of sources associated with older stellar populations has a steeper slope than the XLF of X-ray sources coinciding with young stellar populations, consistent with theoretical predictions.

*Subject headings:* galaxies: individual (NGC 300) — galaxies: spiral — X-rays: galaxies: luminosity function

## 1. INTRODUCTION

The X-ray emission from normal, non-active galaxies originates from a mixture of stellar sources and hot, diffuse gas. In spiral galaxies, this X-ray emission is dominated by X-ray binaries (XRBs) comprising either a neutron star (NS) or a black hole (BH) accreting from a stellar companion. The fast evolutionary timescale of massive stars ( $\sim 10^7$  years) makes X-ray emission from high-mass XRBs (HMXBs) nearly simultaneous with their formation (Shtykovskiy & Gilfanov 2007), while the longer-lived low-mass XRB (LMXB) systems trace older underlying stellar populations (Kong et al. 2002; Soria & Kong 2002; Trudolyubov et al. 2002); thus, the age and star formation history (SFH) of the host galaxy should correlate with the shape of the X-ray luminosity function (XLF) (Grimm et al. 2003; Belczynski et al. 2004; Eracleous et al. 2006). Dependencies of the XRB population properties on host galaxy metallicity may provide useful constraints on binary evolution and population synthesis models.

With its excellent angular resolution ( $\sim 0''.5$ ) and positional accuracy, the *Chandra X-ray Observatory* is the only X-ray telescope capable of separating the X-ray point source populations of nearby galaxies from diffuse emission. When combined with deep, optical *Hubble*

*Space Telescope (HST)* imaging, reliable source identification and optical counterpart identification may be carried out even at distances of a few Mpc. The *Chandra* Local Volume Survey (CLVS, P.I. Benjamin Williams) is a deep, volume-limited X-ray survey of five nearby galaxies (NGC 55, NGC 300, NGC 404, NGC 2403, and NGC 4214) with matched *HST* observations down to  $M_V \sim 0$  (Dalcanton et al. 2009). When combined with the already well-studied disks of M 31 (Kong & Di Stefano 2003) and M 33 (Williams et al. 2008; Plucinsky et al. 2008; Tüllmann et al. 2011), these galaxies contain  $\sim 99\%$  of the stellar mass and  $\sim 90\%$  of the recent star formation out to a distance of  $\sim 3.3$  Mpc (Tikhonov et al. 2005; Maíz-Apellániz et al. 2002; Freedman & Madore 1988). Additionally, these galaxies span a representative sample of disk galaxies with a range of masses, metallicities, and morphologies.

In this paper, we present the results of a new *Chandra* observation of the nearby SA(s)d spiral galaxy NGC 300, located at a distance of 2.0 Mpc (Dalcanton et al. 2009) in the Sculptor Group. NGC 300 is a near-optical twin of the Local Group galaxy M 33, and has a low foreground Galactic absorption of  $4.09 \times 10^{20} \text{ cm}^{-2}$  (Kalberla et al. 2005) and is viewed at an inclination angle  $i = 42^\circ$ ; Table 1 lists some basic properties of NGC 300, as well as M 33 and the Milky Way for direct comparison.

The first X-ray population studies of NGC 300 were performed with *ROSAT* between 1991 and 1997 (Read & Pietsch 2001), identifying 29 bright X-ray sources including NGC 300 X-1, a highly variable supersoft source, and other bright sources coincident with known supernova remnants (SNRs) and H II regions. More recently, an *XMM-Newton* survey of the the X-ray source population of NGC 300 was presented by Carpano et al. (2005) down to a limiting luminosity of  $\sim 3 \times 10^{35}$  erg s<sup>−1</sup> in the

<sup>1</sup> University of Washington, Department of Astronomy, Box 351580, Seattle, WA 98195

<sup>2</sup> Department of Astronomy & Astrophysics, The Pennsylvania State University, 525 Davey Lab, University Park, PA 16802

<sup>3</sup> Harvard-Smithsonian Center for Astrophysics, 60 Garden Street Cambridge, MA 02138, USA

<sup>4</sup> University of Minnesota, Astronomy Department, 116 Church St. SE, Minneapolis, MN 55455

<sup>5</sup> Institute of Astronomy and Department of Physics, National Tsing Hua University, Hsinchu 30013, Taiwan

TABLE 1  
SUMMARY OF NGC 300 PROPERTIES

Property (1)	NGC 300 (2)	M 33 (3)	Milky Way (4)
Distance	2.0 Mpc <sup>a</sup>	800 kpc <sup>b</sup>	8.5 kpc
Type	SA(s)d <sup>c</sup>	SA(s)cd <sup>c</sup>	SBc
$M_B$	-17.66 <sup>a</sup>	-18.4 <sup>d</sup>	-20.3 <sup>h</sup>
Scale length (kpc)	1.3 <sup>e</sup>	1.4 <sup>e</sup>	3.00±0.22 <sup>h</sup>
Circular velocity	97 km s <sup>-1</sup> <sup>f</sup>	130 km s <sup>-1</sup> <sup>g</sup>	239±5 km s <sup>-1</sup> <sup>h</sup>
Estimated stellar mass	4.3 × 10 <sup>9</sup> M <sub>⊙</sub> <sup>f</sup>	4.5 × 10 <sup>9</sup> M <sub>⊙</sub> <sup>g</sup>	6.43 ± 0.63 × 10 <sup>10</sup> M <sub>⊙</sub> <sup>h</sup>

NOTE. — <sup>a</sup>Dalcanton et al. (2009); <sup>b</sup>Williams et al. (2009); <sup>c</sup>NED; <sup>d</sup>Vila-Costas & Edmunds (1992); <sup>e</sup>Muñoz-Mateos et al. (2007); <sup>f</sup>Puche et al. (1990); <sup>g</sup>Corbelli & Salucci (2000); <sup>h</sup>McMillan (2011)

0.3-6 keV band. A total of 163 sources were detected in the energy range of 0.3-6 keV, and the 86 sources falling within the  $D_{25}$  optical disk were further characterized using hardness ratios, X-ray fluxes, and the available ground-based optical imaging. A brief summary of previous X-ray NGC 300 studies is provided in Table 2.

Before the publication of the full *Chandra* X-ray point source catalog, our collaboration employed this new observation of NGC 300 to study two individual objects of interest: the “supernova impostor” SN 2010da, which we argued is consistent with a Be-X-ray binary (BeXB, comprised of a young, rapidly rotating B-type star with strong emission lines and a NS) origin (Binder et al. 2011b), and the BH + Wolf-Rayet binary NGC 300 X-1 (Binder et al. 2011a). These sources are included as part of the X-ray source catalog, but are not discussed in detail in this work.

The organization of this paper is as follows: in Section 2 we provide the details of our new observation, data reduction procedure, and the technique used to generate the X-ray source catalog. An analysis of the X-ray source catalog, including comparisons to previous studies, hardness ratios, and the radial source distribution is given in Section 3. In Section 4, we present a new X-ray/optical source classification scheme, identify candidate optical counterparts to our X-ray sources, and assign likely source classifications (HMXB, LMXB, SNR, or background AGN) to each source. The X-ray luminosity function, and the possible role of transient sources in determining the luminosity function shape, is discussed in Section 5. The paper concludes with a summary and the main conclusions in Section 6.

## 2. OBSERVATIONS AND DATA REDUCTION

### 2.1. Observations

NGC 300 was observed on 2010 September 25 for 63 ks using ACIS-I during the *Chandra* X-ray Observatory Cycle 12, observation ID 12238. Data reduction was carried out with CIAO v4.3 and CALDB v4.4.2 using standard reduction procedures. Images were created with bin sizes of 1, 2, 3, and 4 pixels for each of the following energy bands: 0.35-8, 0.35-1, 1-2, and 2-8 keV. Exposure maps were constructed using *mkinstmap* and *mkexpmap* in CIAO. Exposure-corrected images were generated using our exposure maps and instrument maps. The instrument maps were created assuming spectral weights appropriate for a power law spectrum typical of XRBs and background AGN ( $\Gamma = 1.9$ ). The average foreground column density  $N_H$  was used.

Figure 1 shows an RGB-rendered X-ray image of

NGC 300, with numerous X-ray sources visible. Soft X-ray emission (0.35-1 keV) is shown in red, medium X-ray emission (1-2 keV) is shown in green, and hard X-ray emission (2-8 keV) is in blue. The  $D_{25}$  isophote is superimposed in white.

Nine *HST* fields were used to search for optical counterparts of each of our X-ray point sources. Three *HST* Advanced Camera for Surveys (ACS, Ford et al. 1998) observations of NGC 300 were taken as part of the ACS Nearby Galaxy Survey Treasury (ANGST, GO-10915) forming a radial strip from the center of the galaxy into the disk, hereafter referred to as ‘WIDE1-3.’ Six additional archival ACS images scattered across the NGC 300 disk (GO-9492) are also included, and labeled as ‘NGC300-1-6.’ Detailed descriptions of the *HST* star catalogs, including photometric measurements and quality cuts, are given in Williams et al. (2009) and Dalcanton et al. (2009), while a thorough discussion of the survey completeness and star formation histories (SFH) of NGC 300 are presented in Gogarten et al. (2010).

Figure 2 shows a ground-based Palomar Observatory Sky Survey (POSS) image of NGC 300, with the locations of the *HST* fields shown in red and our *Chandra* field superimposed in blue. The locations of the *Chandra*-detected X-ray point sources (see §3) are shown by green crosses.

### 2.2. Image Alignment

To classify optical counterparts to our *Chandra* X-ray sources, we place both the *Chandra* and *HST* frames onto the International Celestial Reference System (ICRS) by finding matches between stars or background galaxies in the Two Micron All Sky Survey (2MASS) Point Source Catalog (Skrutskie et al. 2006). We performed relative astrometry by individually aligning each *HST* and *Chandra* field to the same reference image frame and coordinate system.

For our reference image, we retrieved a publicly-available ground-based *R* band image (see Larsen & Richtler 2000, for more details) of NGC 300 from NED. Foreground 2MASS stars with ground-based *R*-band counterparts were identified, and we used the IRAF task *ccmap* to compute the plate solution and update the image header with corrected WCS information. By using the 2MASS stars as reference, the astrometric solution yielded root-mean-square (*r.m.s.*) residuals of 0''.00773 in right ascension and 0''.0225 in declination relative to the 2MASS astrometry for the ground-based *R*-band image.

We were next able to align each of our *HST* frames and our *Chandra* frame to the 2MASS-aligned ground-

TABLE 2  
SUMMARY OF PRIOR X-RAY SURVEYS OF NGC 300

Observatory	Number of Detected Sources (within $D_{25}$ )	Limiting Unabsorbed Luminosity ( $10^{36} \text{ erg s}^{-1}$ ) <sup>a</sup>	References
(1)	(2)	(3)	(4)
<i>ROSAT</i>	47 (29)	$\sim 4.0$ ( $\sim 7.7$ )	Read & Pietsch (2001)
<i>XMM-Newton</i>	163 (86)	$\sim 0.3$ ( $\sim 0.4$ )	Carpano et al. (2005)
<i>Chandra</i>	95 (77)	1.5	this work

NOTE. — <sup>a</sup>The limiting unabsorbed luminosities correspond to the 0.1-2.4 keV and 0.3-6.0 keV energy ranges for *ROSAT* and *XMM-Newton*, respectively. In parenthesis we provide expected 0.35-8 keV limiting unabsorbed luminosity assuming a power law with  $\Gamma = 1.9$  and  $N_H = 4.09 \times 10^{20} \text{ cm}^{-2}$ .

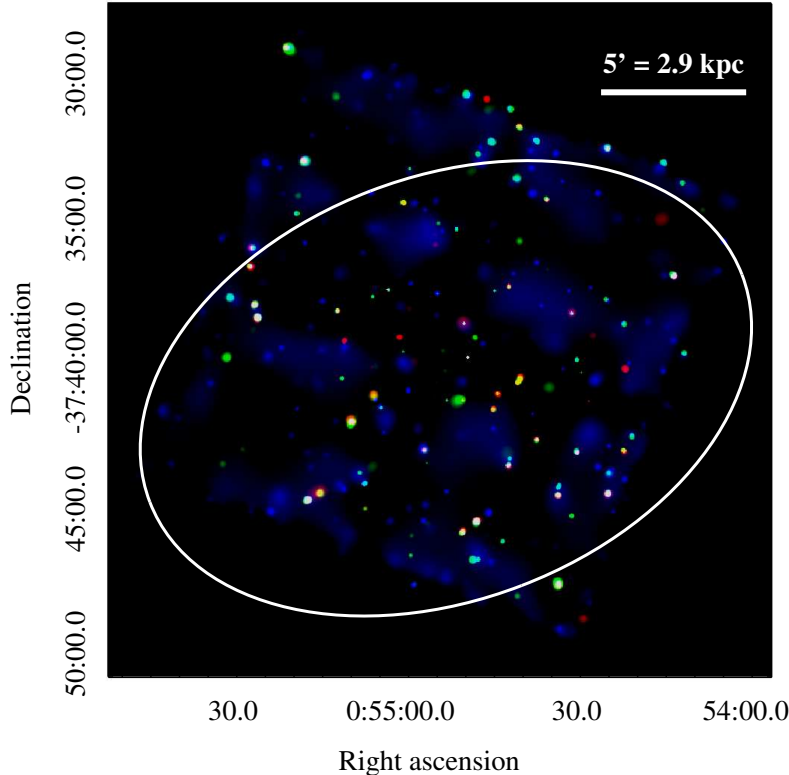


FIG. 1.— An RGB rendering of our *Chandra* exposure of NGC 300. Soft X-ray emission (0.35-1 keV) is shown in red, medium X-ray emission (1-2 keV) is shown in green, and hard X-ray emission (2-8 keV) is in blue. The white outline shows the  $D_{25}$  isophote.

based *R*-band image. For each *HST* field, we identified potential matches between the ground-based *R*-band image and the *F814W* frames; we typically were able to match 3-8 stars per *HST* frame. The plate solutions were again computed using *ccmap*, with *r.m.s.* residuals typically less than a few hundredths of an arcsecond in both right ascension and declination. The *Chandra* field was searched for X-ray sources that matched the positions of foreground stars or background galaxies in 2MASS. Five sources were identified, and we obtained *r.m.s.* residuals of  $0''.13$  in right ascension and  $0''.26$  in declination. The total alignment error for each field was computed by summing in quadrature the *r.m.s.* residuals in the individual fields and the ground-based *R*-band image. The results of our 2MASS astrometry are summarized in Table 3.

### 2.3. Source Catalog Creation

We employed the same source detection strategy described by Tüllmann et al. (2011) in the *Chandra* ACIS

Survey of M 33 (ChASem33) source catalog. We present a summary of the approach here; the reader is referred to ChASem33 work for further details. The CIAO task *wavdetect* (Freeman et al. 2002) was first used to create a list of potential source candidates. The positions of these potential sources was then used as input to *ACIS-Extract* (AE; Broos et al. 2010), a source extraction and characterization tool. AE was used to determine various source properties (source and background count rates, detection significances, etc.) in multiple, user-defined energy bands. Additionally, AE extracts spectra (with appropriate response matrices) and examines source light curves for temporal variability (see Broos et al. 2010, for details). The Poisson probability of not being a source (*prob\_no\_source*; hereafter *pns*) is provided by AE for each source (taking the local background uncertainty into account). We use these *pns* values as our source significance threshold criteria when constructing the NGC 300 X-ray point source catalog.

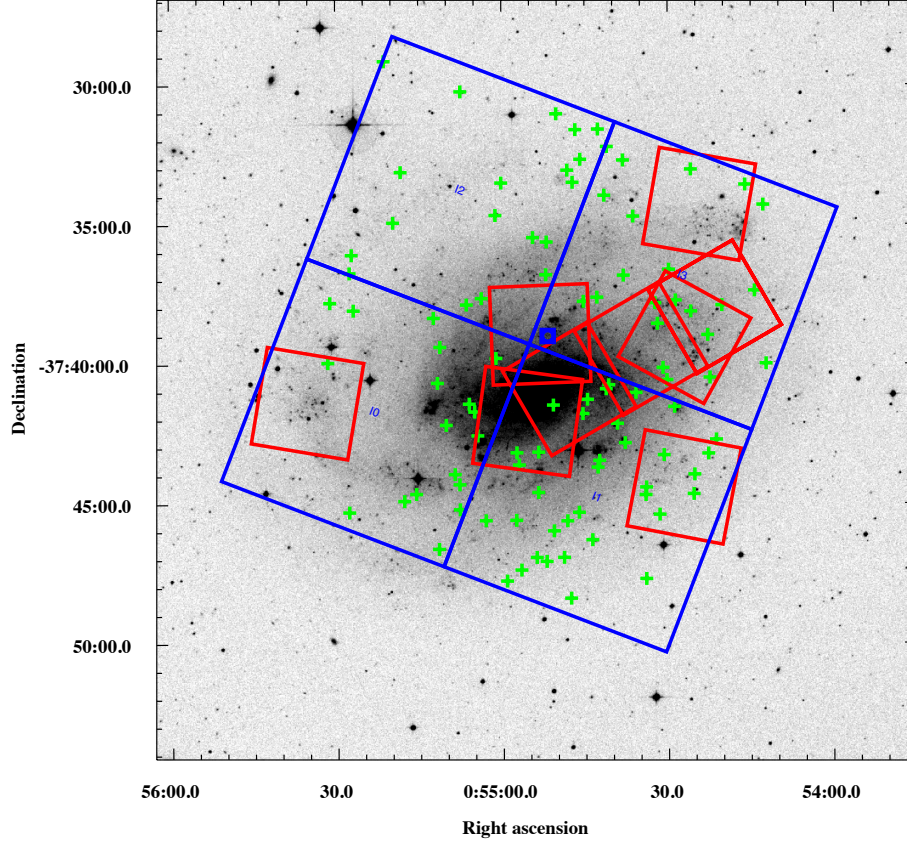


FIG. 2.— A POSS image of NGC 300, with the *HST* fields shown in red and our *Chandra* field of view superimposed in blue. The locations of our X-ray point sources are shown by green crosses.

TABLE 3  
ALIGNMENT OF *Chandra* AND *HST* IMAGES TO 2MASS

Description	Observation ID	R.A. (J2000)	Decl. (J2000)	# Sources Used For Alignment	<i>r.m.s.</i> , R. A. <sup>a</sup>	<i>r.m.s.</i> , Decl. <sup>a</sup>	# of X-ray Sources
(1)	(2)	(3)	(4)	(5)	(6)	(7)	(8)
ground-based <i>R</i>				4	0'00773	0'0225	
<i>Chandra</i>	12238	00:54:53.05	-37:38:42.1	5	0'1332 (0'1330)	0'2580 (0'2570)	95
Wide-1	10915	00:54:21.37	-37:37:56.3	5	0'0518 (0'0512)	0'0400 (0'0327)	5
Wide-2	10915	00:54:34.7	-37:39:25.2	4	0'0171 (0'0152)	0'0342 (0'0258)	6
Wide-3	10915	00:54:47.7	-37:40:51.6	4	0'0171 (0'0152)	0'0535 (0'0485)	5
NGC 300-1 <sup>b</sup>	9492	00:55:35.66	-37:41:25.2	3	0'0340 (0'0331)	0'0421 (0'0356)	1
NGC 300-2	9492	00:54:52.96	-37:38:59.8	6	0'0772 (0'0768)	0'0435 (0'0372)	2
NGC 300-3	9492	00:54:55.33	-37:42:04.5	4	0'0179 (0'0162)	0'0263 (0'0137)	5
NGC 300-4	9492	00:54:24.42	-37:34:20.8	5	0'0528 (0'0522)	0'0449 (0'0388)	2
NGC 300-5	9492	00:54:26.89	-37:39:01.4	8	0'0230 (0'0217)	0'0441 (0'0379)	9
NGC 300-6	9492	00:54:27.12	-37:44:23.2	4	0'0253 (0'0241)	0'0400 (0'0331)	7

NOTE. —

<sup>a</sup>Alignment errors listed show the uncertainties in each individual field and the ground-based *R*-band image added in quadrature. The error in parentheses is the uncertainty reported by `cmap` for the individual field.

<sup>b</sup>Used `rxyscale`.

Our initial source list was deliberately generated with many more sources than we anticipated being statistically significant. We then applied an iterative procedure to remove sources with increasing significance thresholds, until only a small number of false sources remained in the final source list. Each time the source list was filtered, the output was visually examined for potentially lost (real) sources. We used the same images described in

Section 2.1 using a variety of binning and energy ranges to create the initial source list: `wavdetect` was run on each energy and bin combination, using *scale* sizes ranging from 1 to 16 in a power-of-two sequence. To generate the initial list of candidate sources, we ran `wavdetect` with the following parameters: the source significance (*sigthresh*) was set to  $10^{-4}$  (to catch all real sources and many false ones), the cleansing threshold (*bkgthresh*)

was set to  $10^{-2}$  (Freeman et al. 2002), and we used maximum number of cleansing iterations (*maxiter*) of 5. Default values were used for all other *wavdetect* parameters. The resulting candidate lists were merged and culled of duplicate sources, resulting in an initial source list comprised of 799 candidate sources.

Low rates of false detections using the *AEpns* threshold criteria result from values below  $\sim 10^{-6}$  (Nandra et al. 2005; Georgakakis et al. 2008; Tüllmann et al. 2011). We adopt a value of *pns* =  $4 \times 10^{-6}$  as our criteria for selecting those sources that are highly probable to be genuine. However, due to the high number of source candidates in our initial list, source crowding posed a serious issue and made defining background regions problematic. To address this issue, the output from our first AE iteration was filtered with *pns* =  $10^{-2}$ . The filtered source list contained revised source properties and improved background estimates. All sources failing to meet this initial *pns* threshold were visually examined, and any obviously missed sources were added back to the candidate source list. The source list resulting from our first iteration contained 224 sources. We then ran AE again on the filtered source list, this time raising the *pns* threshold to  $10^{-3}$ . Source crowding was again reduced and spurious sources were filtered out, yielding an output list of 129 potential sources. Again, sources failing to meet our new *pns* criteria were visually examined and returned to the source list if necessary.

AE was run a final time on the resulting source list, and the *pns* value was computed in each of the following nine energy bands (in keV): 0.5-8, 0.5-2, 2-8, 0.5-1, 1-2, 2-4, 4-8, 0.35-1, and 0.35-8. To be included in the final NGC 300 catalog, a source was required to have a *pns* value less than  $4 \times 10^{-6}$  in *any* of the nine energy bands; if only the 0.35-8 keV band were considered,  $\sim 4\%$  of significant sources would have been lost. The final CLVS source catalog for NGC 300 contains 95 sources<sup>6</sup>. Their positions and properties, such as detection significance (*pns* value), net counts, and photon flux (in eight different energy bands) are listed in Tables 4-7.

#### 2.4. Sensitivity Maps

AE provides an estimate of the photon flux (*flux2*) based on the net number of source counts (*net\_cnts*), the exposure time, and the mean ARF in the given energy band. To convert this photon flux into an energy flux, knowledge of the intrinsic X-ray spectrum is required – however, less than 20% of the NGC 300 X-ray sources have a sufficiently large number of counts that can be used to constrain a spectral model.

To enable a uniform comparison between NGC 300 and M33, we adopt the same approach as employed by Tüllmann et al. (2011): we assume an absorbed power law spectrum, with  $\Gamma = 1.9$  and  $N_H = 4.09 \times 10^{20} \text{ cm}^{-2}$ , to estimate the energy flux for each source. This model is hereafter referred to as the “standard model,” and appears to be reasonable for both XRBs associated with NGC 300 as well as for background AGN (especially at low flux levels). We note that the energy flux estimate for individual sources may be off by as much as a factor of two if the true spectrum is different from our assumed

one, although the net effect of this assumption is not expected to systematically bias the  $\log N$ - $\log S$  relation to higher or lower fluxes.

The following analyses require, for each point in our *Chandra* exposure, a sensitivity map which provides the energy flux level at which a source would be detectable. The CIAO task *lim\_sens* was used to compute limiting sensitivity maps from the background image, exposure map, and ACIS-I PSF image. Our 90% complete limiting luminosities in the 0.35-8 keV, 0.5-2 keV, and 2-8 keV ranges are  $1.5 \times 10^{36} \text{ erg s}^{-1}$ ,  $8.8 \times 10^{35} \text{ erg s}^{-1}$ , and  $4.1 \times 10^{36} \text{ erg s}^{-1}$ , respectively. Table 8 summarizes the limiting luminosities for the 70%, 90%, and 95% completeness levels for our total energy range, the soft band, and the hard band.

### 3. THE X-RAY SOURCE CATALOG

Various properties of individual X-ray sources, such as their temporal variability or spectral shape, can be used to constrain the physical origin of the X-ray emission. Additionally, bulk population properties (i.e., radial source distribution and the XLF) allow us to discriminate between those sources associated with NGC 300 and background AGN in a statistical sense. We expect the observable X-ray point source population of NGC 300 to be comprised of HMXBs, LMXBs, background AGN, and a few bright supernova remnants (SNRs). To match each point source to its most likely physical origin, we use our catalog to identify time-variable sources, analyze hardness ratios (for faint sources) and spectra (for sufficiently bright sources), and create XLFs. The additional matched *HST* optical observations allow us to identify candidate optical counterparts and measure correlations between the X-ray emission and the underlying stellar age as a function of radius of NGC 300.

#### 3.1. Comparison with XMM-Newton and Temporal Variability

Some classes of XRBs, as well as background AGN, exhibit long-term X-ray variability on timescales of months to years, while SNRs and some HMXBs will show persistent X-ray emission. To search for long-term variability, we compared our *Chandra* X-ray catalog to the *XMM-Newton* survey conducted by Carpano et al. (2005), which contained 86 sources within the  $D_{25}$  isophote of NGC 300. We consider sources with X-ray positional offsets  $< 3''.5$  to be matches.

To correct for the differences in energy ranges between *Chandra* (0.35-8 keV) and *XMM-Newton* (0.3-6 keV), we converted all *XMM-Newton* fluxes into *Chandra* fluxes assuming our standard model. Due to the differences in energy resolution, detector efficiencies, etc., we cannot compare *Chandra* and *XMM-Newton* hardness ratios to search for changes in spectral shape (see Section 3.2 for further discussion of source hardness ratios). Tüllmann et al. (2011) defined a variability threshold as  $\eta = (\text{flux}_{\text{max}} - \text{flux}_{\text{min}}) / \Delta \text{flux}$ , where the flux error  $\Delta \text{flux}$  is calculated using the Gehrels approximation (appropriate for low count data; Gehrels 1986), to identify sources with potential long-term variability. Any source with  $\eta \geq 5$  is considered potentially variable; according to this criteria, 8 sources in the NGC 300 catalog exhibit long-term variability. Table 9 lists the temporal variability measurements for the 52 sources observed by both

<sup>6</sup> Source catalogs are available in FITS format at: <http://www.astro.washington.edu/users/bbinder/CLVS/>

TABLE 4  
NGC 300 SOURCE LIST

Source No.	Source ID	R.A. (J2000) ( $^{\circ}$ )	Decl. (J2000) ( $^{\circ}$ )	Positional Error ( $''$ )	Total exp. map value (s cm $^2$ )	$R_{\text{src}}$ (sky pixel)	$\theta$ ( $^{\circ}$ )
(1)	(2)	(3)	(4)	(5)	(6)	(7)	(8)
1	005411.98-373951.8	13.549937	-37.664408	0.70	$1.589 \times 10^7$	13.43	8.2
2	005412.31-373359.6	13.551319	-37.566583	0.93	$1.434 \times 10^7$	16.66	9.3
3	005413.98-373710.5	13.558268	-37.619588	0.36	$1.588 \times 10^7$	12.14	7.9
4	005415.57-373316.4	13.564907	-37.554563	0.59	$1.210 \times 10^7$	15.25	9.2
5	005419.92-373744.5	13.583001	-37.629032	0.61	$1.711 \times 10^7$	8.49	6.6

NOTE. — Column 2: the source ID also contains the source coordinates (J2000.0). Column 5: the positional uncertainty is a simple error circle (in  $''$ ) around R.A. and decl. Column 6: sum of mean exposure map values in the source region. Column 7: the average radius of the source extraction region (1 sky pixel =  $0''.392$ ). Column 8: off-axis angle. Only the first five entries are shown.

TABLE 5  
LOGARITHMIC  $pns$  VALUES FOR DIFFERENT ENERGY BANDS

Source No.	$\log(pns)$ [1] (0.5-8.0 keV)	$\log(pns)$ [2] (0.5-2.0 keV)	$\log(pns)$ [3] (2.0-8.0 keV)	$\log(pns)$ [4] (0.35-8.0 keV)	$\log(pns)$ [5] (0.35-1.1 keV)	$\log(pns)$ [6] (1.1-2.6 keV)	$\log(pns)$ [7] (2.6-8.0 keV)	$\log(pns)$ [8] (0.35-2.0 keV)
(1)	(2)	(3)	(4)	(5)	(6)	(7)	(8)	(9)
1	-9.32	-8.60	-3.16	-9.13	<-10	<-10	-2.05	-2.05
2	-4.54	-3.57	-2.17	-4.81	-0.42	-2.80	-2.77	-2.77
3	<-10	<-10	<-10	<-10	<-10	<-10	-6.03	-6.03
4	<-10	<-10	-6.94	<-10	-3.46	<-10	-4.76	-4.76
5	-5.48	-4.58	-2.15	-6.04	-3.20	-3.49	-1.41	-1.41

NOTE. — The (logarithmic)  $pns$  value is the Poisson probability of not being a source.  $\log(pns)$  values smaller than -10 have been replaced by <-10. All these cases are highly significant detections. Only the first five entries are shown.

TABLE 6  
TOTAL NET COUNTS IN DIFFERENT ENERGY BANDS

Source No.	$net\_cnts$ [1] (0.5-8.0 keV)	$net\_cnts$ [2] (0.5-2.0 keV)	$net\_cnts$ [3] (2.0-8.0 keV)	$net\_cnts$ [4] (0.35-8.0 keV)	$net\_cnts$ [5] (0.35-1.1 keV)	$net\_cnts$ [6] (1.1-2.6 keV)	$net\_cnts$ [7] (2.6-8.0 keV)	$net\_cnts$ [8] (0.35-2.0 keV)
(1)	(2)	(3)	(4)	(5)	(6)	(7)	(8)	(9)
1	$22.9^{+6.6}_{-5.5}$	$13.3^{+5.0}_{-3.8}$	$9.6^{+5.0}_{-3.9}$	$22.8^{+6.6}_{-5.5}$	< 1.1	$17.1^{+5.5}_{-4.3}$	$6.4^{+4.5}_{-3.3}$	$13.2^{+5.0}_{-3.8}$
2	$17.3^{+6.5}_{-5.4}$	$8.3^{+4.5}_{-3.3}$	$9.1^{+5.4}_{-4.3}$	$18.2^{+6.6}_{-5.5}$	$0.7^{+2.7}_{-1.3}$	$7.5^{+4.5}_{-3.3}$	$9.9^{+5.3}_{-4.1}$	$9.1^{+4.6}_{-3.4}$
3	$70.9^{+9.8}_{-8.8}$	$45.6^{+7.9}_{-6.8}$	$25.3^{+6.6}_{-5.5}$	$70.8^{+9.8}_{-8.8}$	$16.5^{+5.2}_{-4.1}$	$40.3^{+7.6}_{-6.5}$	$14.0^{+5.4}_{-4.2}$	$45.6^{+7.9}_{-6.8}$
4	$45.3^{+8.5}_{-7.4}$	$25.5^{+6.3}_{-5.2}$	$19.8^{+6.3}_{-5.2}$	$45.1^{+8.5}_{-7.4}$	$6.0^{+3.8}_{-2.6}$	$24.6^{+6.2}_{-5.1}$	$14.5^{+5.7}_{-4.6}$	$25.3^{+6.3}_{-5.2}$
5	$11.2^{+4.9}_{-3.7}$	$6.3^{+3.8}_{-2.6}$	$4.9^{+3.8}_{-2.6}$	$12.1^{+5.0}_{-3.8}$	$3.7^{+3.2}_{-1.9}$	$5.2^{+3.6}_{-2.4}$	$3.2^{+3.4}_{-2.2}$	$7.2^{+4.0}_{-2.8}$

NOTE. — Only the first five entries are shown.

TABLE 7  
PHOTON FLUX (PHOTONS CM $^{-2}$  s) IN DIFFERENT ENERGY BANDS

Source No.	$\log(flux)$ [1] (0.5-8.0 keV)	$\log(flux)$ [2] (0.5-2.0 keV)	$\log(flux)$ [3] (2.0-8.0 keV)	$\log(flux)$ [4] (0.35-8.0 keV)	$\log(flux)$ [5] (0.35-1.1 keV)	$\log(flux)$ [6] (1.1-2.6 keV)	$\log(flux)$ [7] (2.6-8.0 keV)	$\log(flux)$ [8] (0.35-2.0 keV)
(1)	(2)	(3)	(4)	(5)	(6)	(7)	(8)	(9)
1	-5.75	-6.11	-6.09	-5.74		-6.07	-6.25	-6.07
2	-5.84	-6.28	-6.08	-5.81	-6.83	-6.40	-6.04	-6.20
3	-5.26	-5.57	-5.67	-5.25	-5.54	-5.69	-5.91	-5.54
4	-5.28	-5.65	-5.60	-5.27	-5.77	-5.74	-5.73	-5.61
5	-6.07	-6.45	-6.39	-6.03	-6.23	-6.60	-6.57	-6.35

NOTE. — Only the first five entries are shown.

*Chandra* and *XMM-Newton*, with sources showing evidence of variability listed in boldface.

We found a total of 75 X-ray sources that were detected by either *Chandra* or *XMM-Newton*, but not both. For these sources, we use the detection limit of the observatory in which the source was not observed to set a lower-limit on the long-term source variability. X-ray transients (XRTs) observed in the Milky Way and other

nearby galaxies originate in either LMXBs or HMXBs, but in all cases the peak X-ray luminosity exceeds the quiescent X-ray luminosity by more than an order of magnitude. We therefore define XRT candidates in NGC 300 as those sources whose maximum luminosity is at least an order of magnitude above the detection limit for the exposure in which they were not observed. The 25 sources meeting this criteria are listed in Table 10.

TABLE 8  
LIMITING LUMINOSITIES FOR OUR NGC 300 OBSERVATION

Energy (keV)	70% ( $10^{35}$ erg s $^{-1}$ )	90% ( $10^{35}$ erg s $^{-1}$ )	95% ( $10^{35}$ erg s $^{-1}$ )
(1)	(2)	(3)	(4)
0.35-8	7.7	15	45
0.5-2	4.5	8.8	27
2-8	21	41	120

TABLE 9  
NGC 300 CROSS IDENTIFICATIONS WITH *XMM-Newton* SOURCES

CLVS Source No.	<i>XMM-Newton</i> Source No. ID	Positional Offset (")	$\xi$	$\eta$	flux $_{\max}$ /flux $_{\min}$
(1)	(2)	(3)	(4)	(5)	(6)
1	41	0.76	0.7958	0.21	1.41
3	17	1.38	0.9152	0.79	2.49
6	45	0.98	0.5160	0.44	1.69
7	39	0.60	0.5590	2.79	4.30
8	42	1.70	0.2267	0.14	1.26

NOTE. — Columns 1 and 2 give the CLVS and *XMM-Newton* source numbers, respectively. Column 3: the difference (in arcseconds) between the CLVS and the *XMM-Newton* source positions. Sources with positional offsets less than  $3''$  are considered matches. Column 4 is the K-S probability of the source being constant within our *Chandra* observation (short-term variability). Sources with K-S probabilities of  $\xi \leq 3.7 \times 10^{-3}$  are likely to show short-term variability and are shown in boldface. Column 5:  $\eta$  is the variability index defined by Tüllmann et al. (2011) and is sensitive to long-term variability; sources with variability indices of  $\eta \geq 5$  are likely to show long-term variability and are shown in boldface. Column 6: variability factor expressed as the ratio of flux $_{\max}$ /flux $_{\min}$ . Only the first five entries are shown.

We additionally searched the *Chandra* source catalog for short-term variability in the 0.35-8 keV band (i.e., variability that occurs on timescales less than the exposure time,  $\sim 18$  hours). We used a Kolmogorov-Smirnov (K-S) test to compare the cumulative photon arrival time distribution for each X-ray source to a uniform count rate model. The K-S test returns a probability that both distributions were drawn from the same underlying distribution. One source (18) has a K-S probability indicating rapid variability at the  $3\sigma$  level.

### 3.2. Hardness Ratios

The X-ray spectrum of a source can provide a key diagnostic for separating different sources. For example, XRBs and AGN are typically well described with power laws with photon indices  $\Gamma = 1.5$ -2.0, while soft X-ray sources (such as SNRs) show spectra consistent with a thermal plasma of temperatures of  $\sim 0.3$ –0.8 keV (Long et al. 2010). Still other sources, such as low luminosity AGN, may exhibit an X-ray spectrum consistent with bremsstrahlung emission (Yi & Boughn 1998). However, in order to constrain the fit parameters of these various models to believable values, a sufficiently high signal-to-noise is required. Even in the best case scenario, low signal-to-noise data (less than  $\sim 50$  counts) can only have a power law photon index constrained to  $\sim 50\%$  accuracy. The majority of the NGC 300 X-ray sources in our catalog fall into this low-count category (see Figure 3).

To assess the X-ray spectral shape for low-count sources, a different approach must be used. Hardness ratios (HRs), also referred to as X-ray colors, are computed for various energy bands to measure the fraction of soft ( $S$ , 0.35-1.1 keV), medium ( $M$ , 1.1-2.6 keV), and hard ( $H$ , 2.6-8.0 keV) photons emitted by a source. A source comprised of a thermally emitted X-rays, such as a SNR, will show characteristically soft X-ray colors, while an obscured background AGN (having had most

of its softer X-rays absorbed) will exhibit a significantly harder X-ray color.

We evaluate two HRs for each source using source and background counts determined by AE in the bands listed above. We define a “soft” color,

$$HR1 = \frac{M - S}{H + M + S}, \quad (1)$$

and a “hard” color,

$$HR2 = \frac{H - M}{H + M + S}. \quad (2)$$

We use the Bayesian Estimation of Hardness Ratios (*BEHR*, Park et al. 2006) in an approach described by Tüllmann et al. (2011) (see also Prestwich et al. 2009) to determine the hardness ratios of the NGC 300 X-ray sources. The *BEHR* code has the advantage of requiring source and background counts to be non-negative (net counts for low-count sources can be negative due to fluctuations in the source and background estimates, resulting in unphysical HRs); however, it cannot directly compute HRs in the form we require. We therefore use the *BEHR* code to generate 50,000 samples of the probability distribution of source fluxes for each energy band. To do this, we use as input to *BEHR* the following quantities from the AE output for each source: source and background counts, the AE “backscale” parameter (to account for the ratio of the source and background extraction areas and efficiencies), and a factor converting from counts to flux (i.e., the exposure time multiplied by the mean of the ARF over the extraction region in the appropriate energy band). We then run the *BEHR* code twice, once for  $S$  and  $M$  and again for  $S$  and  $H$ .

We combine the results from our two *BEHR* runs to obtain 50,000 values of  $HR1$  and  $HR2$  for each source. Because the difference of two Poisson distributions does



TABLE 10  
CANDIDATE TRANSIENT X-RAY SOURCES FROM *Chandra* AND *XMM-Newton*

Source No. <sup>a</sup>	R.A. (J2000)	Decl. (J2000)	$\eta^b$	flux <sub>max</sub> /flux <sub>min</sub> <sup>b</sup>
(1)	(2)	(3)	(4)	(5)
CXO-4	13.564907	-37.554563	16.11	21.76
CXO-12	13.605871	-37.546400	11.52	15.84
CXO-24	13.641366	-37.796388	15.37	24.81
CXO-29	13.657195	-37.542294	9.94	12.50
CXO-33	13.669315	-37.534468	32.23	42.53
CXO-44	13.689520	-37.542735	12.91	18.54
CXO-52	13.707457	-37.515847	12.24	17.26
CXO-73	13.770201	-37.695464	13.49	20.47
CXO-76	13.779925	-37.504917	8.33	10.63
CXO-87	13.825446	-37.553972	12.92	18.80
CXO-89	13.837805	-37.488834	41.25	68.58
XMM-2	13.795250	-37.809556	13.80	403.83
XMM-3	13.709708	-37.647083	21.06	594.39
XMM-4	13.795458	-37.648417	11.15	85.26
XMM-5	13.669417	-37.680250	5.39	57.76
XMM-8	13.835292	-37.802833	3.86	35.67
XMM-10	13.835292	-37.643944	6.35	60.56
XMM-16	13.706458	-37.666861	5.55	51.68
XMM-18	13.700292	-37.782611	5.00	43.24
XMM-23	13.583208	-37.652472	4.15	30.07
XMM-25	13.926000	-37.673250	5.91	28.49
XMM-43	13.722000	-37.722000	3.27	18.90
XMM-52	13.566292	-37.566292	2.92	12.68
XMM-53	13.807708	-37.807708	3.27	12.51
XMM-59	13.849958	-37.756694	3.28	12.29

NOTE. — <sup>a</sup>Sources labeled as ‘CXO’ were detected in our *Chandra* catalog only; sources labeled as ‘XMM’ were detected in the Carpano et al. (2005) *XMM-Newton* catalog only.

<sup>b</sup>The long-term variability index  $\eta$  and the variability factor flux<sub>max</sub>/flux<sub>min</sub> listed are lower limits.

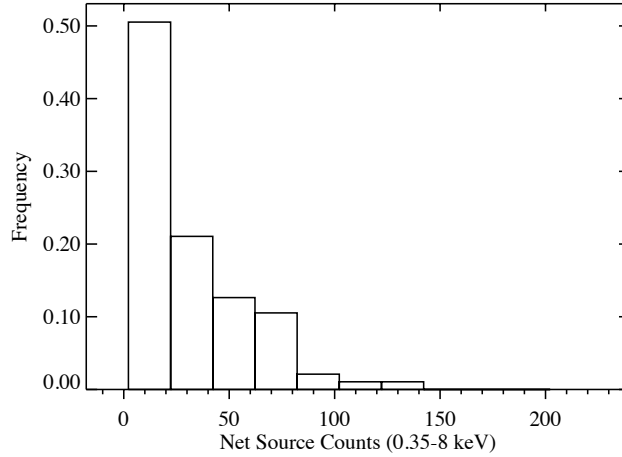


FIG. 3.— Histogram of the net counts observed in the 0.35-8 keV band for our NGC 300 X-ray catalog, excluding source 80 (NGC 300 X-1). We find the majority of our sources have less than 50 counts, making spectral modeling for these sources unreliable.

not follow Poisson statistics, we do not use the error estimates directly provided by these *BEHR* runs. Instead, the HR value is defined as the mean of the distribution, and the credible interval is evaluated based on the 68.2% equal-tail estimates (i.e., 0.682/2 of the samples have values below the lower limit, and 0.682/2 of the samples have values above the upper limit). Our HRs for each source are listed in Table 11.

To aid in the interpretation of our HR calculations, we employ an X-ray color-color classification scheme similar to that used in Kilgard et al. (2005). Due to the

differences in energy bands considered in this work, we modify the classification scheme slightly. We simulated spectra for thermal sources of varying temperature (0.1-2 keV) and power law sources (with  $\Gamma = 0.4-3$ ) with different levels of absorption and calculated HR1 and HR2 for each source to inform our X-ray color cuts. We define six categories: XRBs (which likely also contain a significant fraction of background AGN), SNRs, absorbed sources (‘ABS’), indeterminate soft sources (‘SOFT’), indeterminate hard sources (‘HARD’), and sources with an indeterminate spectral type (labeled ‘INDET’, although



TABLE 11  
X-RAY SOURCE HARDNESS RATIOS

Source No.	HR1	HR2	Class
(1)	(2)	(3)	(4)
1	$0.72 \pm 0.25$	$-0.71 \pm 0.32$	ABS
2	$0.19 \pm 0.41$	$-0.09 \pm 0.51$	XRB
3	$0.36 \pm 0.13$	$-0.56 \pm 0.12$	SOFT
4	$0.50 \pm 0.15$	$-0.47 \pm 0.21$	ABS
5	$-0.07 \pm 0.46$	$-0.15 \pm 0.35$	XRB

NOTE. — Only the first five entries are shown.

we do not observe any sources with hardness ratios fitting this criteria). Indeterminate sources are those whose X-ray spectra are ambiguous; for example, ‘HARD’ sources may have exceptionally flat power law spectra, suffer extreme absorption, have multiple spectral components that cannot be distinguished due to our low number of source counts, or some combination of these effects. The color-color classification scheme is summarized in Table 12, and a plot of the HRs for the NGC 300 X-ray source population is shown in Figure 4.

We find most of the NGC 300 sources fall within the ‘XRB’ category (41%), and an additional  $\sim 12\%$  of sources are categorized as SNRs. This is not surprising – X-ray emission from non-active spiral galaxy with recent star formation is expected to be dominated by XRBs and bright SNRs. Nearly one-third of the NGC 300 X-ray sources show evidence for absorption beyond the Galactic column. Two sources exhibit unusually hard X-ray colors, and are likely background AGN whose soft X-ray emission has suffered a high degree of absorption. Thirteen sources show unusually soft X-ray colors. These may be very soft XRBs, sources with unusual absorption, or foreground objects not associated with NGC 300.

### 3.3. X-ray Spectral Analysis

As discussed above, the X-ray spectrum of a source depends on the physical X-ray production mechanism. The value of the spectral fit parameters can reveal further clues to the nature of the X-ray emission. For example, XRBs containing a NS primary will show a hard power law with  $\Gamma \sim 1 - 1.5$ , while BH primaries produce a significantly softer spectrum with  $\Gamma \sim 2 - 2.5$ .

AE utilizes the CIAO tools `dmextract`, `mkacisrmf`, and `mkarf` when extracting spectra and generating response products. Due to the low number of counts found for most of the sources in our catalog, we fit spectral models to the unbinned spectra and use  $C$ -statistics in lieu of traditional  $\chi^2$  statistics. The only X-ray source to have more than 200 net counts in the 0.35-8 keV band is source 80, the HMXB NGC 300 X-1. Detailed spectral fitting and timing analysis was carried out for this source in Binder et al. (2011a).

The ungrouped spectra for 53 of the 95 sources were automatically fit in AE with one of four models: a power-law model, an APEC model (Smith et al. 2001), or either a power-law or thermal model with additional absorption. The `tbabs` model (Wilms et al. 2000) was used to model the Galactic absorption ( $N_H = 4.09 \times 10^{20} \text{ cm}^{-2}$ ; Kalberla et al. 2005). To determine the best-fit model, we first rejected those models which predicted unreasonably high photon indices ( $\Gamma > 4$ ) or plasma temperatures ( $kT > 6 \text{ keV}$ ). To assign a goodness-of-fit comparison for each of the models using  $C$ -statistics, we used XSPEC’s

`goodness` command to perform 5,000 Monte Carlo calculations of the goodness-of-fit for each model. The command simulated spectra based on the model and computed the fraction of simulations with a fit statistic less than that found for the data – if the observed spectrum was produced by that model, the `goodness` should be around 50%. We therefore chose the best-fit model as the one for which the `goodness` command returned closest to 50%. In some cases, the `goodness` command returned values near 50% for multiple models, or did not return a reasonable value for any model. In these cases, we checked each spectrum for indications for emission features. In cases where evidence of thermal emission was present, the thermal model (with fixed  $N_H$ ) was adopted; for all other sources, the power law with fixed  $N_H$  was chosen. The best-fit model and parameters for sources in NGC 300 with greater than 50 net counts are listed in Table 13.

### 3.4. Radial Source Distribution

We assign an inclination-corrected galactocentric distance to each X-ray sources assuming the following galaxy parameters for NGC 300, as in Gogarten et al. (2010):  $\alpha_0 = 13^\circ 722833$ ,  $\delta_0 = -37^\circ 684389$  (galaxy center),  $i = 42^\circ$ , (inclination), and  $\theta = 111^\circ$  (position angle Kim et al. 2004). The maximum radius we find for an X-ray source in our *Chandra* field is  $r = 8.06 \text{ kpc}$ .

We divide the X-ray sources into radial bins based on their inclination-corrected distance from the center of the galaxy. The bins are spaced 0.9 kpc apart in radius so that we can directly compare the X-ray radial distribution to the stellar population analysis presented in Gogarten et al. (2010). We use the cumulative  $\log N$ - $\log S$  distribution of Cappelluti et al. (2009) to estimate the expected contamination by background AGN, which should be nearly flat with galactocentric radius.

The radial X-ray source distribution is shown in Figure 5, and clearly shows that the number of X-ray sources per square kiloparsec decreases with galactocentric radius. Since NGC 300 does not possess a substantial bulge, we fit the background-subtracted radial X-ray source distribution to a simple exponential profile, and find the best-fit relation to be

$$\mathcal{N}_X(r) = (12.8 \pm 3.0)e^{-r/(1.7 \pm 0.2)} - (0.57 \pm 0.85), \quad (3)$$

where  $\mathcal{N}_X(r)$  is the number of X-ray sources per  $\text{kpc}^2$  expected at a given galactocentric radius,  $r$  (in kpc). The exponential scale length is  $1.7 \pm 0.2 \text{ kpc}$ , similar to the  $1.3 \pm 0.1 \text{ kpc}$  scale length found by Gogarten et al. (2010) and in excellent agreement with estimates derived from the  $K$ -band surface brightness (Muñoz-Mateos et al.

TABLE 12  
HARDNESS RATIO SOURCE CLASSIFICATION SCHEME

Classification (1)	Definition (2)	# Sources (3)
X-ray binary ('XRB')	$-0.4 < HR2 < 0.4, -0.4 < HR1 < 0.4$	39
Absorbed source ('ABS')	$HR1 > 0.4$	30
Supernova remnant ('SNR')	$HR2 < 0.4, HR1 < -0.4$	11
Indeterminate hard source ('HARD')	$HR2 > 0.4, -0.4 < HR1 < 0.4$	2
Indeterminate soft source ('SOFT')	$HR2 < -0.4, -0.4 < HR1 < 0.4$	13

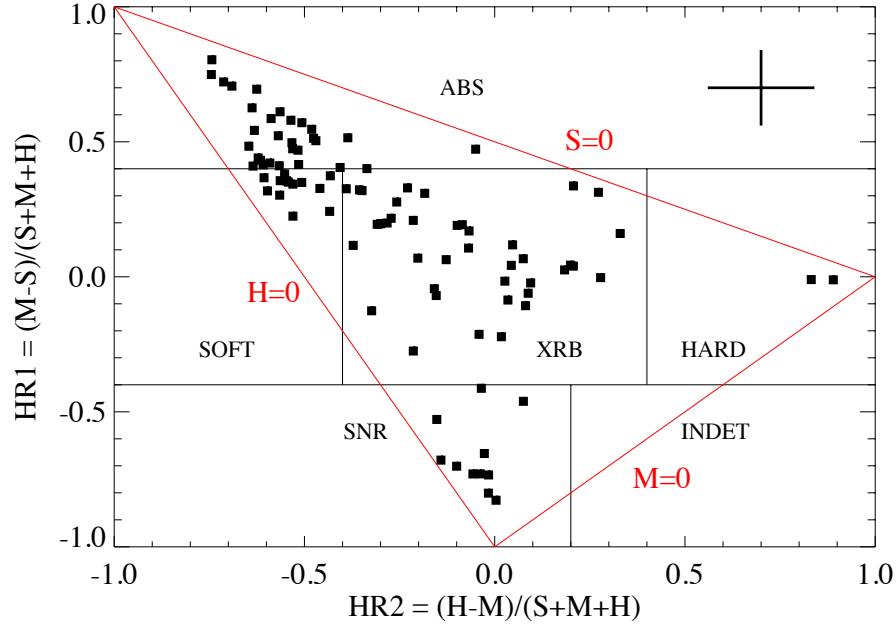


FIG. 4.— X-ray color-color diagrams of all X-ray sources detected in NGC 300. The thick cross in the upper-right corner shows the typical size of the errors. The diagram has been broken into preliminary source identification regions, described in Table 12. The regions are labeled as: ‘ABS’ for absorbed sources, ‘XRB’ for X-ray binaries, ‘SNR’ for supernova remnants, ‘SOFT’ for indeterminate soft sources, ‘HARD’ for indeterminate hard sources, and ‘INDET’ for sources with an indeterminate spectral shape (although we do not observe any sources in this category). The red lines indicate the zero-count limits in the hard (‘H’), medium (‘M’), and soft (‘S’) bands.

2007). We additionally find the X-ray scale length to be consistent with multiwavelength measurements. The radial source distribution suggests that the X-ray sources in NGC 300 are the evolutionary end-points of a parent population of disk stars.

For an exponential disk, we expect 90% of stars to be inside of 4 kpc (6'.9), suggesting that the majority of sources beyond this radius are not associated with the stellar disk of NGC 300. This suggests that 37 X-ray sources beyond 4 kpc are likely to be AGN (i.e., 40% of the sample). This interpretation is consistent with the estimated number of background and hard sources identified in our hardness ratio analysis.

We use the source classifications determined by our hardness ratio analysis to investigate the differences in galactocentric radii among the different types of sources. The results are summarized in Table 14. We find both the preliminary SNR and XRB candidates to have median radii less than 4 kpc, suggesting that many of these are indeed associated with NGC 300. However, XRB-classified sources span a wide range of galactocentric radii (out to 6.7 kpc). Given that background AGN are antic-

ipated to dominate the X-ray sources at greater than  $\sim 4$  kpc, the ‘XRB’ class likely suffers from AGN contamination. ‘SOFT’ sources additionally span a wide range in radii, with a median distance of 4 kpc, suggesting that at least some of these sources are likely to be associated with NGC 300. Absorbed and indeterminate hard sources have median galactocentric radii greater than 4 kpc, implying that many of these sources are background or foreground objects.

#### 4. SOURCE CLASSIFICATION

##### 4.1. Supernova Remnants

In Section 3.2, we found that 11 X-ray sources in our catalog had hardness ratios consistent with those of SNRs. Of these, only one source (#43) had a sufficient number of counts for spectral modeling to be performed. Source 43 was best-fit by a thermal plasma model with a temperature  $kT=0.4$  keV, consistent with SNRs observed in M33 (Long et al. 2010). Taking this as our “standard SNR” model, we estimate the unabsorbed 0.5-2 keV luminosities for the remaining 10 SNR candidates and find a range in luminosities of  $\sim 5 \times 10^{35}$  lum to  $\sim 6 \times 10^{36}$

TABLE 13  
BEST-FIT SPECTRAL MODELS FOR SOURCES WITH MORE THAN 50 COUNTS

No.	Best-fit <sup>a</sup> Model	$N_H$ <sup>b</sup> ( $\text{cm}^{-2}$ )	$\Gamma$	$kT$ (keV)	Norm <sup>c</sup>	$dof$ <sup>d</sup>	$C$	$L_X$ (0.5-2.0 keV) <sup>e</sup> ( $10^{36} \text{ erg s}^{-1}$ )	$L_X$ (0.5-8.0 keV) <sup>f</sup> ( $10^{36} \text{ erg s}^{-1}$ )	“goodness <sup>g</sup> ” (%)
(1)	(2)	(3)	(4)	(5)	(6)	(7)	(8)	(9)	(10)	
3	pow	...	$1.7 \pm 0.3$	...	$3.12 \times 10^{-6}$	1016	576.19	$3.3 \pm 1.1$	$8.5^{+3.3}_{-2.1}$	45.38
11	pow	...	$1.5 \pm 0.4$	...	$2.39 \times 10^{-6}$	1016	625.87	$2.6 \pm 0.7$	$8.0^{+2.2}_{-1.8}$	82.80
23	pow	$0.7^{+0.6}_{-0.4}$	$2.2^{+0.9}_{-0.7}$	...	$1.10 \times 10^{-5}$	1016	464.43	$2.7^{+1.1}_{-0.9}$	$10.3^{+4.2}_{-3.3}$	32.70
24	apec	...	...	$4.8^{+20.7}_{-2.7}$	$1.22 \times 10^{-5}$	1016	750.98	$3.4^{+0.9}_{-0.9}$	$7.9^{+1.8}_{-3.8}$	98.38
25	pow	$<0.4$	$2.3^{+1.4}_{-0.7}$	...	$4.42 \times 10^{-6}$	1016	385.29	$3.2^{+1.9}_{-1.0}$	$6.2^{+3.8}_{-1.9}$	55.28
28	pow	$<0.4$	$1.4 \pm 0.2$	...	$2.17 \times 10^{-6}$	1016	438.60	$2.4 \pm 0.7$	$8.2^{+2.7}_{-2.0}$	44.54
33	pow	$0.2^{+0.5}_{-0.2}$	$1.8^{+0.9}_{-0.7}$	...	$6.99 \times 10^{-6}$	1015	679.83	$7.4^{+2.6}_{-7.0}$	$16.7^{+3.3}_{-10.5}$	55.04
35	pow	$1.1^{+1.0}_{-0.5}$	$1.3^{+0.7}_{-0.4}$	...	$6.66 \times 10^{-6}$	1015	706.75	$7.4^{+1.0}_{-2.8}$	$27.5^{+6.1}_{-10.9}$	41.04
39	pow	...	$1.5 \pm 0.4$	...	$2.29 \times 10^{-6}$	1016	590.38	$2.5^{+0.7}_{-0.5}$	$7.7^{+2.5}_{-1.8}$	64.26
43	apec	...	...	$0.4 \pm 0.1$	$1.92 \times 10^{-5}$	1016	456.08	$6.8^{+1.2}_{-1.7}$	$6.8^{+1.2}_{-1.4}$	66.84
50	pow	...	$1.6 \pm 0.3$	...	$4.12 \times 10^{-6}$	1016	631.44	$4.4^{+0.8}_{-0.9}$	$12.3^{+3.0}_{-2.1}$	91.80
52	pow	$0.9^{+0.9}_{-0.6}$	$2.5^{+1.7}_{-1.1}$	...	$8.22 \times 10^{-6}$	1016	390.55	$1.6^{+1.1}_{-0.7}$	$5.7^{+3.9}_{-2.5}$	55.88
53	pow	$<0.3$	$2.1^{+1.0}_{-0.4}$	...	$3.31 \times 10^{-6}$	1016	380.30	$3.5^{+1.7}_{-0.7}$	$6.7^{+3.2}_{-1.3}$	52.93
87	apec	$<0.2$	...	$2.6^{+1.5}_{-0.8}$	$7.31 \times 10^{-6}$	1016	371.56	$2.7^{+1.6}_{-0.8}$	$5.0^{+2.9}_{-1.5}$	72.86
89	pow	$0.3^{+0.4}_{-0.3}$	$2.4^{+0.6}_{-0.5}$	...	$1.62 \times 10^{-5}$	1015	564.66	$17.3^{+4.0}_{-12.0}$	$27.7^{+7.0}_{-12.7}$	71.14
95	apec	...	...	$0.6^{+0.8}_{-0.3}$	$1.79 \times 10^{-6}$	1016	541.01	$0.7^{+0.3}_{-0.6}$	$0.7^{+0.5}_{-0.6}$	98.80

NOTE. —

<sup>a</sup> The best-fit model is either a **powerlaw** or **vappec** model, depending on which one has the lower  $C/dof$ .

<sup>b</sup> Intrinsic source absorption (in units of  $10^{22} \text{ cm}^{-2}$ ), if beyond the Galactic column was required.

<sup>c</sup> Normalization constant of the fit, in units of photons  $\text{keV}^{-1} \text{ cm}^{-2} \text{ s}^{-1}$  and  $\text{cm}^{-5}$  for the power law and thermal plasma models, respectively.

<sup>d</sup> Degrees of freedom.

<sup>e,f</sup> Unabsorbed X-ray luminosities, assuming a distance to NGC 300 of 2.0 Mpc (Dalcanton et al. 2009).

<sup>g</sup> Results of the XSPEC “goodness” command, run using 5000 realizations.

TABLE 14  
GALACTOCENTRIC RADII BY HARDNESS RATIO IDS

Source classification	$r_{\min}$ (kpc)	$r_{\max}$ (kpc)	$r_{\text{av}}$ (kpc)
(1)	(2)	(3)	(4)
SNR	0.4	6.0	2.5
XRB	1.3	6.7	3.4
ABS	1.2	8.1	4.1
SOFT	2.1	6.2	4.0
HARD	2.8	6.9	4.9

$\text{erg s}^{-1}$ , also consistent with observations of M33 SNRs.

To see if any of our SNR candidates have been previously identified, we cross-correlated our 11 sources with the multiwavelength NGC 300 SNR catalogs of Blair & Long (1997) and Pannuti et al. (2000) and the catalog of NGC 300 H II regions of Deharveng et al. (1988). We find 7 of our 11 sources are located within  $3''.5$  of a SNR or H II region, and two of our X-ray sources are coincident with optically confirmed SNRs. Table 15 summarizes our SNR candidates. Figure 6 shows  $0.5 \times 0.5$  postage stamp images of the H $\alpha$  emission coincident with each X-ray source, with the soft 0.35-1 keV X-ray contours superimposed.

#### 4.2. Optical Counterparts

We searched for optical counterpart candidates for each X-ray source that was contained within one or more overlapping *HST* field. For many of the X-ray sources, we found multiple optical counterpart candidates within the *Chandra* X-ray error circle (typically on the order of  $\sim 0''.5$ ); in these cases, the optical counterpart candidates are labeled ‘a,’ ‘b,’ ‘c,’ etc. in order of increasing dis-

tance away from the X-ray source location. We kept only those optical sources that met the quality cuts described in Williams et al. (2009) and Gogarten et al. (2010) (i.e., sources with sufficient signal-to-noise, not flagged as unusable, meeting predetermined crowding and sharpness thresholds, etc.).

For each source, we compute a logarithmic X-ray-to-optical flux ratio  $\log(f_X/f_V)$ , where  $f_X$  is the 2-10 keV X-ray flux and the  $f_V$  is the optical flux measured in either *F555W* or *F606W*, whichever is available. Although the *F606W* has a slightly larger bandpass than the *F555W* filter, we estimate that for the majority of stars accessible in our *HST* exposures the affect on  $\log(f_X/f_V)$  will be small,  $\sim 0.1$ .

Table 16 lists the optical and X-ray properties of all the X-ray source candidate optical counterparts. Figure 7 shows RGB-rendered  $5'' \times 5''$  finding charts for each of the 32 X-ray sources with overlapping *HST* fields. The X-ray source position is shown by a white cross, with a white circle indicating the extent of the *Chandra* error circle. Red lines are used to indicate the likely optical counterpart; in cases of multiple optical counterparts, the

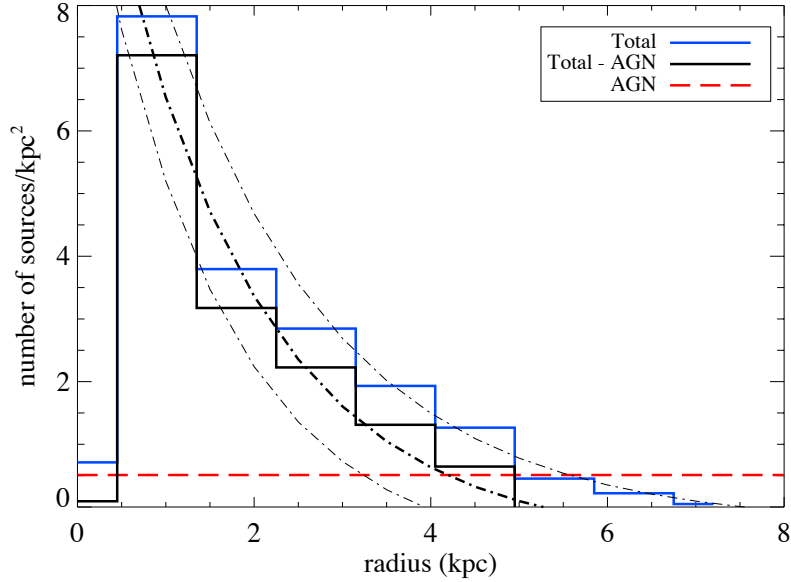


FIG. 5.— The galactocentric source density profile of NGC 300 in the 0.35-8.0 keV band. The blue histogram shows the total number of sources per square kiloparsec. The red dashed line shows the anticipated number of background AGNs, while the black histogram shows the expected number of sources after correcting for background AGNs. The thick dot-dashed line shows our exponential fit to the AGN-subtracted radial source distribution, with the lighter dot-dashed lines indicating the  $1\sigma$  uncertainty.

TABLE 15  
CANDIDATE SUPERNOVA REMNANTS AND H II REGIONS

Source No.	Counterpart	Separation	0.5-2 keV unabs. luminosity ( $\text{erg s}^{-1}$ )	Notes
(1)	(2)	(3)	(4)	(5)
7	SNR	2''6	$6.9 \times 10^{35}$	Blair & Long (1997)
15	H II	3''2	$6.4 \times 10^{35}$	Deharveng et al. (1988)
32			$1.1 \times 10^{36}$	
34	SNR	3''3	$1.5 \times 10^{36}$	Blair & Long (1997), opt. identified Deharveng et al. (1988)
	H II	0''6		
41			$1.5 \times 10^{36}$	
43	SNR	2''8	$5.6 \times 10^{36}$	Pannuti et al. (2000)
46			$6.3 \times 10^{35}$	
54	SNR	3''0	$1.8 \times 10^{36}$	Pannuti et al. (2000)
77			$7.5 \times 10^{35}$	
81	H II	3''1	$4.7 \times 10^{35}$	Deharveng et al. (1988)
85	SNR	0''3	$2.5 \times 10^{36}$	Blair & Long (1997), opt. identified
	H II	3''4		Deharveng et al. (1988)

optical sources are labeled.

Two of the X-ray sources (4 and 8) were coincident with a saturated foreground star and the disk of a background galaxy (with one visible point source nearly coincident with the X-ray position), respectively. Since both of these optical sources failed to meet the *HST* quality criteria of a stellar object in NGC 300, they were not included in the *HST* star catalogs. We used the IRAF task `imexamine` to estimate the magnitudes of the foreground star, the whole background galaxy, and the point source within the X-ray error circle centered on the disk of the background galaxy. The foreground star and background galaxy magnitudes were found to be consistent with those available in SIMBAD. Multi-band photometric measurements for each of the optical counterpart candidates to the X-ray sources are given in Table 16. Source 4 is discussed further in §4.3.1.

#### 4.3. X-ray/Optical Source Classifications

The detection of optical counterpart candidates for each X-ray source with overlapping *HST* fields allows some sources to be assigned a source classification based on their multiwavelength properties. However, many X-ray sources are faint or do not have optical coverage, making their physical nature ambiguous. We therefore attempt to combine statistical quantities (i.e., using the radial source distribution, location in spiral arms, inter-arm regions, or background regions) with individual source properties (variability, X-ray spectral shape, and optical colors) to determine the most likely source classification.

We first consider the statistical properties of each X-ray source. For example, an X-ray source with a galactocentric radius less than 4 kpc that is coincident with a spiral arm is likely to be associated with NGC 300, while

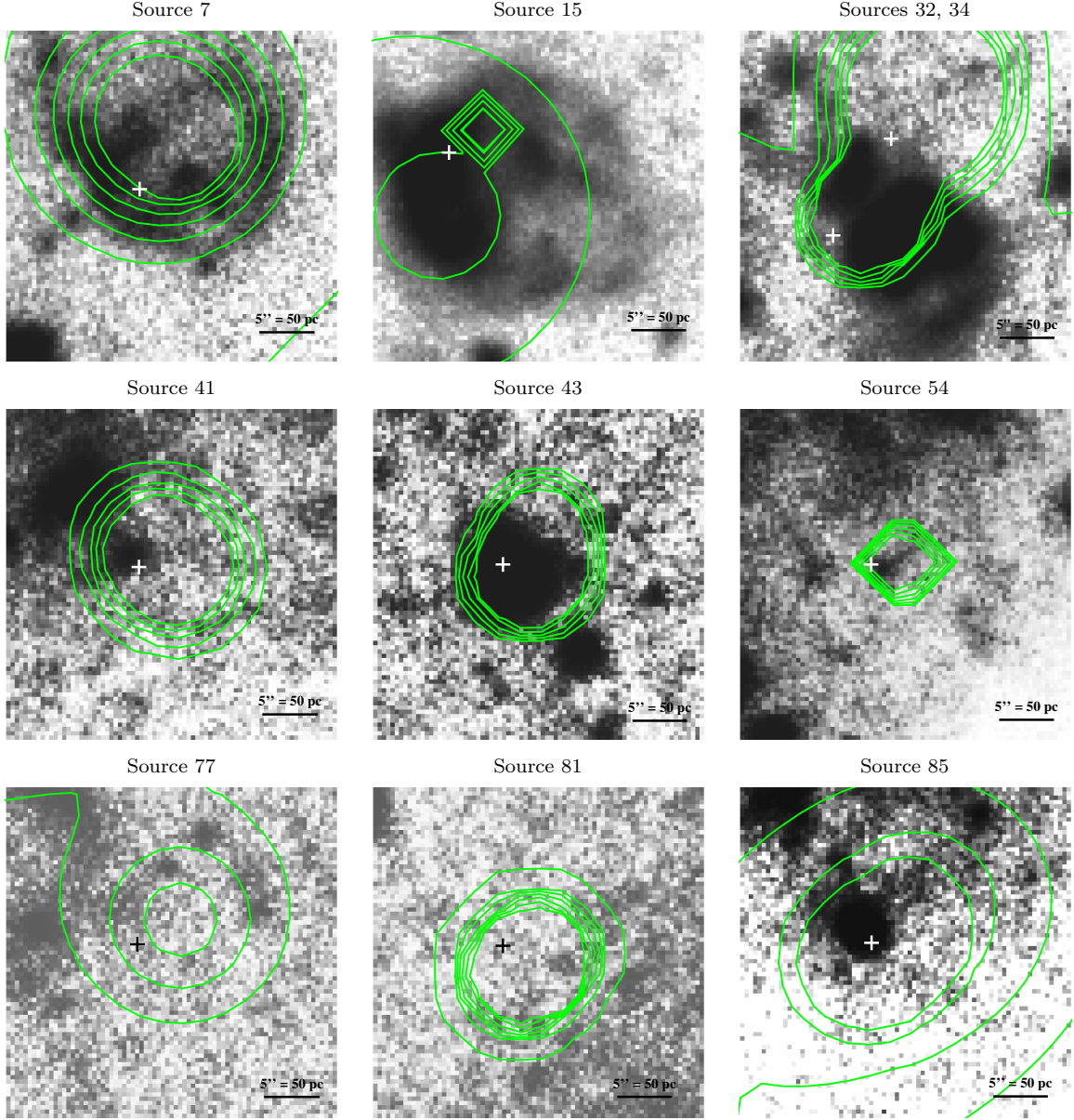


FIG. 6.—  $H\alpha$  emission from each of our SNR candidates (except source 46, for which  $H\alpha$  imaging is not available). Each postage stamp is  $0.5 \times 0.5$ , centered on the apparent  $H\alpha$  emission. Crosses indicate the *Chandra* X-ray source position (determined by the 0.35–8 keV emission). The green contours show the 0.35–1 keV X-ray emission.

an X-ray source at a large galactocentric radius that is not obviously associated with NGC 300 is likely to be a background object. As described in Section 3.4, we expect the majority of X-ray sources at radii beyond 4 kpc are not associated with the stellar disk of NGC 300. We then examined ground-based, optical  $R$ -band and  $H\alpha$  images to identify spiral arms and inter-arm regions in NGC 300, and define background regions not obviously associated with NGC 300. All sources with  $r > 4.5$  kpc ( $\theta > 7.7$ ) were located in ‘background’ regions according to the ground-based imaging, making these sources probable background AGN.

We next consider the individual X-ray properties of each source. Long-term X-ray variability is observed for both AGN and XRBs. However, SNRs and some HMXB systems do not show significant X-ray variability (i.e., NGC 300 X-1; see Binder et al. 2011a, and references

therein). We therefore do not discount the possibility of an XRB nature for non-variable sources. The data on galactocentric radius, location relative to NGC 300, and X-ray variability is then combined with the preliminary source classifications defined using our hardness ratio analysis (see Section 3.2). For sources without overlapping *HST* exposures, we then assign a likely source classification based on our X-ray observations. For example: a source with  $r = 1$  kpc, located within a spiral arm, no significant long-term X-ray variability, and a soft X-ray spectral shape is classified as a likely SNR.

To determine a likely source classification for X-ray sources with overlapping *HST* fields, we generated color-magnitude diagrams (CMDs) of each *HST* field and candidate optical counterparts were classified as falling either on the main sequence (MS) or red giant branch (RGB). Additionally, we constructed X-ray color-



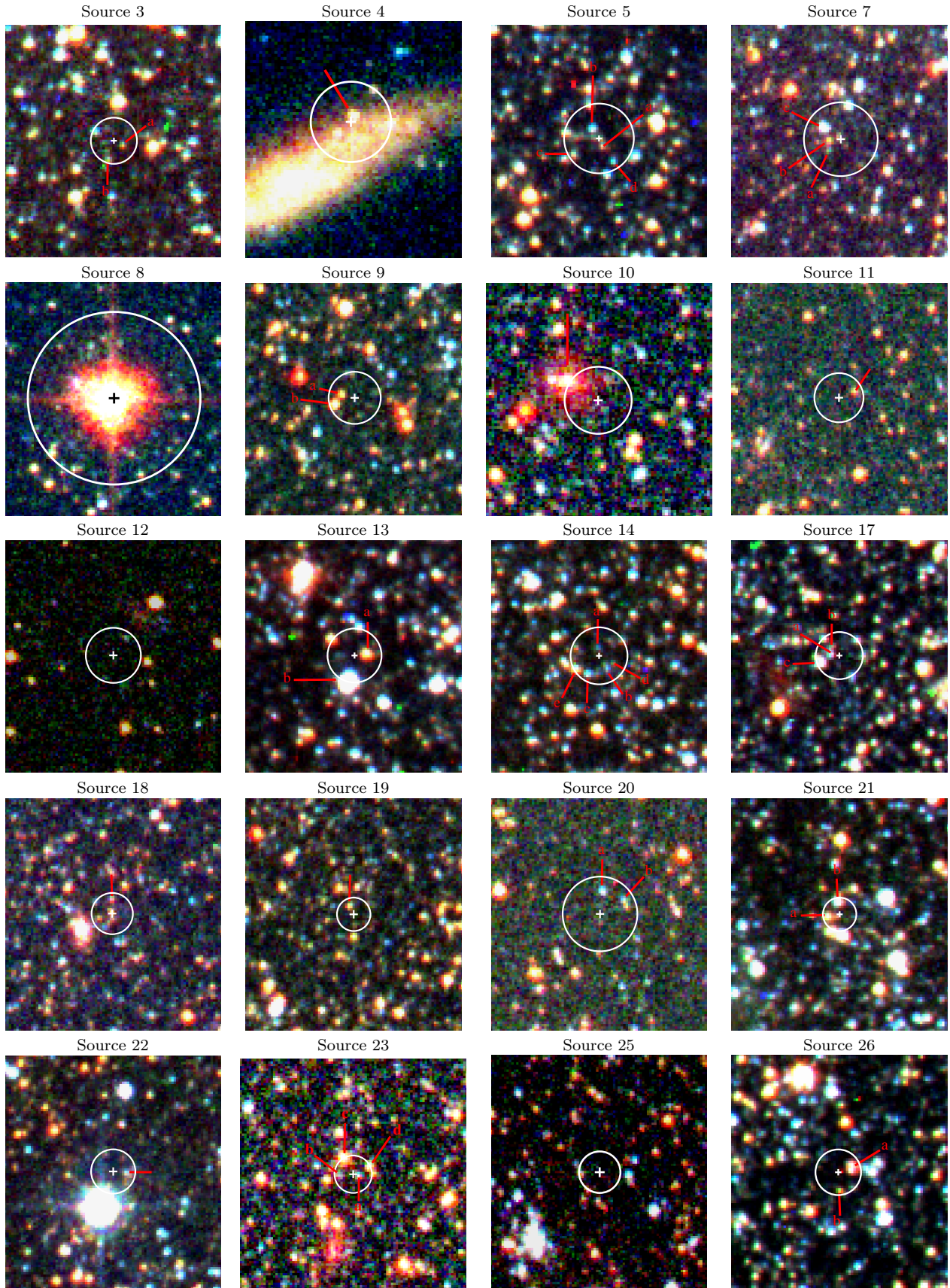


FIG. 7.— Optical RGB-rendered finding charts at the location of each X-ray source, indicated by a cross. White circles show the radius of the 90% *Chandra* error circle for each source. Candidate optical counterparts are indicated with red lines. X-ray sources with multiple candidate optical counterparts have their optical counterparts labeled ‘a,’ ‘b,’ ‘c,’ etc.

TABLE 16  
OPTICAL COUNTERPARTS TO *Chandra* X-RAY SOURCES

Source Name (1)	$d^a$ (arcsec) (2)	$F435W$ (3)	$F475W$ (4)	$F555W$ (5)	$F606W$ (6)	$F814W$ (7)	$f_X^b$ ( $10^{-15}$ erg s $^{-1}$ cm $^{-2}$ ) (8)	$\log(f_X/f_V)^c$ (9)
4 (galaxy)	1''46	21.9		20.3		18.5		-0.24
4 (point source)	0''18	24.7		23.8		23.7	12.0	1.17
5a	0''22		26.99 $\pm$ 0.10		26.39 $\pm$ 0.06	25.47 $\pm$ 0.08		1.44
5b	0''27	25.45 $\pm$ 0.05	25.51 $\pm$ 0.03	25.47 $\pm$ 0.05	25.60 $\pm$ 0.03	25.53 $\pm$ 0.07, 25.86 $\pm$ 0.08	2.1	1.07 (1.12)
5c	0''62		26.86 $\pm$ 0.09		26.17 $\pm$ 0.05	25.42 $\pm$ 0.05		1.35
5d	0''70		26.24 $\pm$ 0.05		26.14 $\pm$ 0.05	26.52 $\pm$ 0.18		1.34
7a	0''39	26.91 $\pm$ 0.14		26.65 $\pm$ 0.12		26.55 $\pm$ 0.14		1.42
7b	0''42	27.13 $\pm$ 0.18		26.93 $\pm$ 0.17		26.13 $\pm$ 0.10	1.6	1.53
7c	0''55	24.04 $\pm$ 0.02		24.13 $\pm$ 0.06		24.25 $\pm$ 0.03		0.41
8	0''04	19.7		18.5		16.6	3.9	-1.44
9a	0''34	27.02 $\pm$ 0.15	26.27 $\pm$ 0.05	25.48 $\pm$ 0.06	25.09 $\pm$ 0.02	23.98 $\pm$ 0.04, 24.04 $\pm$ 0.02	2.7	1.19 (1.04)
9b	0''39	25.98 $\pm$ 0.07	25.43 $\pm$ 0.03	24.75 $\pm$ 0.03	24.40 $\pm$ 0.01	23.51 $\pm$ 0.04, 23.53 $\pm$ 0.02		0.90 (0.76)

NOTE. — <sup>a</sup>The positional offset from the *Chandra* X-ray source location.

<sup>b</sup>X-ray flux is unabsorbed in the 0.35-8 keV energy band.

<sup>c</sup> $f_V$  is calculated from either the  $F555W$  or  $F606W$  magnitude, depending on which is available for a given observation. Only the first five X-ray sources with optical counterpart candidates are listed.



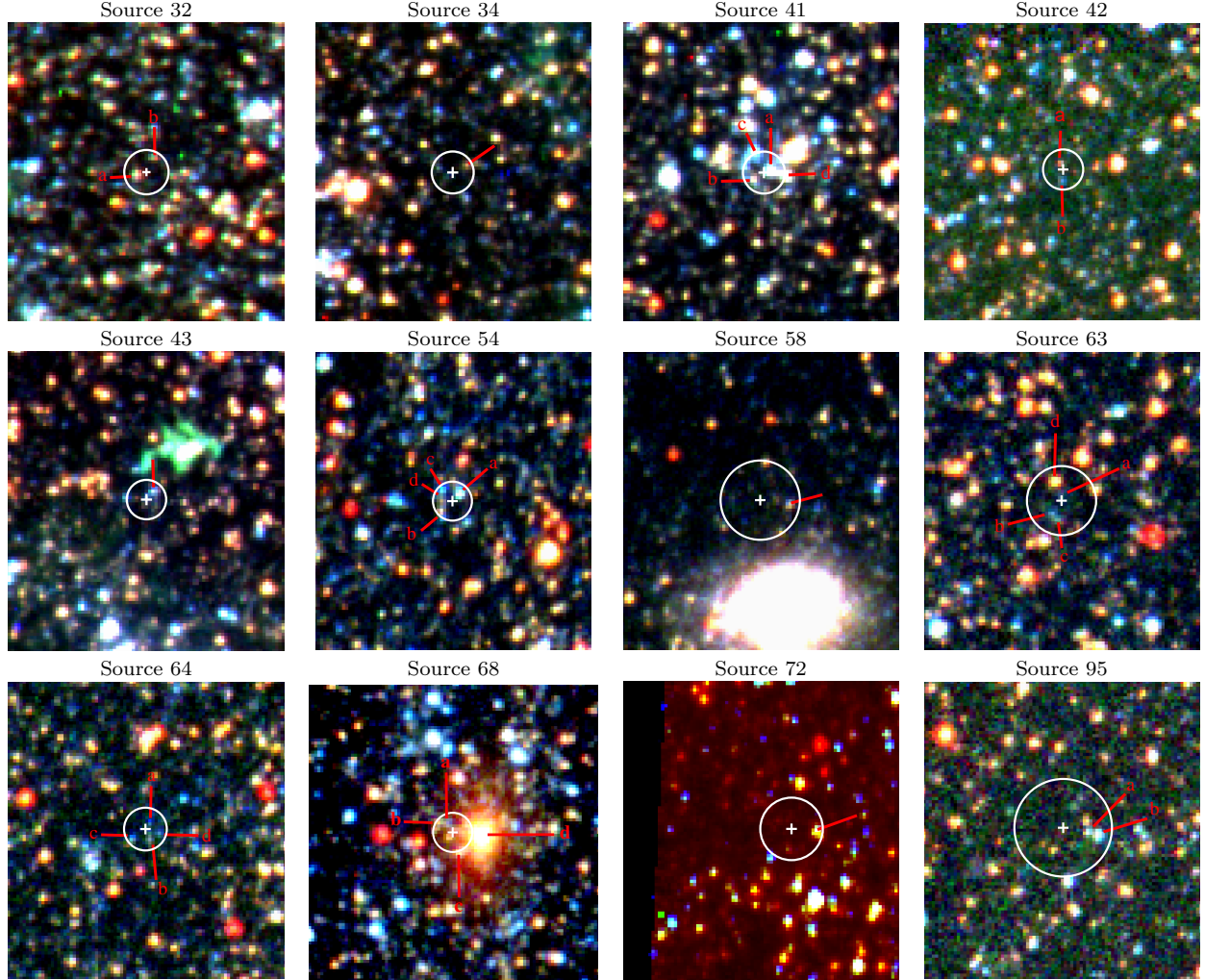


FIG. 7.— (continued) Optical RGB-rendered finding charts at the location of each X-ray source, indicated by a cross. White circles show the radius of the 90% *Chandra* error circle for each source. Candidate optical counterparts are indicated with red lines. X-ray sources with multiple candidate optical counterparts have their optical counterparts labeled ‘a,’ ‘b,’ ‘c,’ etc.

magnitude diagrams (XCMDs), where the optical color was plotted as a function of  $\log(f_X/f_V)$ . Many authors have utilized optical and X-ray colors in discriminating between XRBs and background AGN (e.g., Hornschemeier et al. 2001; Shtykovskiy & Gilfanov 2005); notably, McGowan et al. (2008) found that known pulsars and HMXBs located in the Small Magellanic Cloud occupied a region of the XCMD bounded by  $B - V \lesssim 0$  and  $f_X/f_V \lesssim 1$ .

Optical counterpart candidates were then compared to the XCMD generated for each *HST* field. Sources with blue optical colors ( $F435W - F555W$  or  $F475W - F606W \lesssim 0.2$ ) and  $\log(f_X/f_V) < 1$  are likely to match a young massive main sequence star and are therefore designated as HMXB candidates. Sources falling in the other region of the XCMD are associated with either red giant branch (RGB) stars or background galaxies, and are therefore classified as either AGNs or LMXBs. For illustration, Figure 8 presents a sample CMD and XCMD for the field ‘NGC300-5’ (top panel) as well as a CMD and XCMD of our X-ray/optical source candidates. The sample CMD was generated using the *HST*  $F435W$  and  $F814W$  catalog magnitudes for all optical sources in the ‘NGC300-5’ field. For illustrative purposes, we have

created a sample XCMD using the mean X-ray flux of sources in the NGC 300 catalog ( $\sim 5 \times 10^{-15}$  erg s $^{-1}$  cm $^{-2}$ , corresponding to  $\sim 2 \times 10^{36}$  erg s $^{-1}$  at the distance of NGC 300). Using this X-ray flux, we calculate a  $\log(f_X/f_V)$  for every optical source in the *HST* ‘NGC300-5’ field. The bottom panels show the magnitudes, colors, and X-ray/optical flux ratios for the candidate optical counterparts only. Regions corresponding to likely main sequence (MS) and RGB stars are labeled on the CMD, and the regions defining likely HMXBs and AGNs are labeled on the XCMD.

In order to combine all the relevant X-ray and optical information available from our *Chandra* and *HST* observations, we constructed an IDL routine called `xclass.pro` to automatically process each X-ray source. The routine reads in an input source file containing all X-ray and optical information (if available), and returns a preliminary source classification. The routine additionally tracks which classification channels were utilized by the input sources. The `xclass.pro` routine is publicly available<sup>7</sup>.

<sup>7</sup> See <http://www.astro.washington.edu/users/bbinder/xclass/>

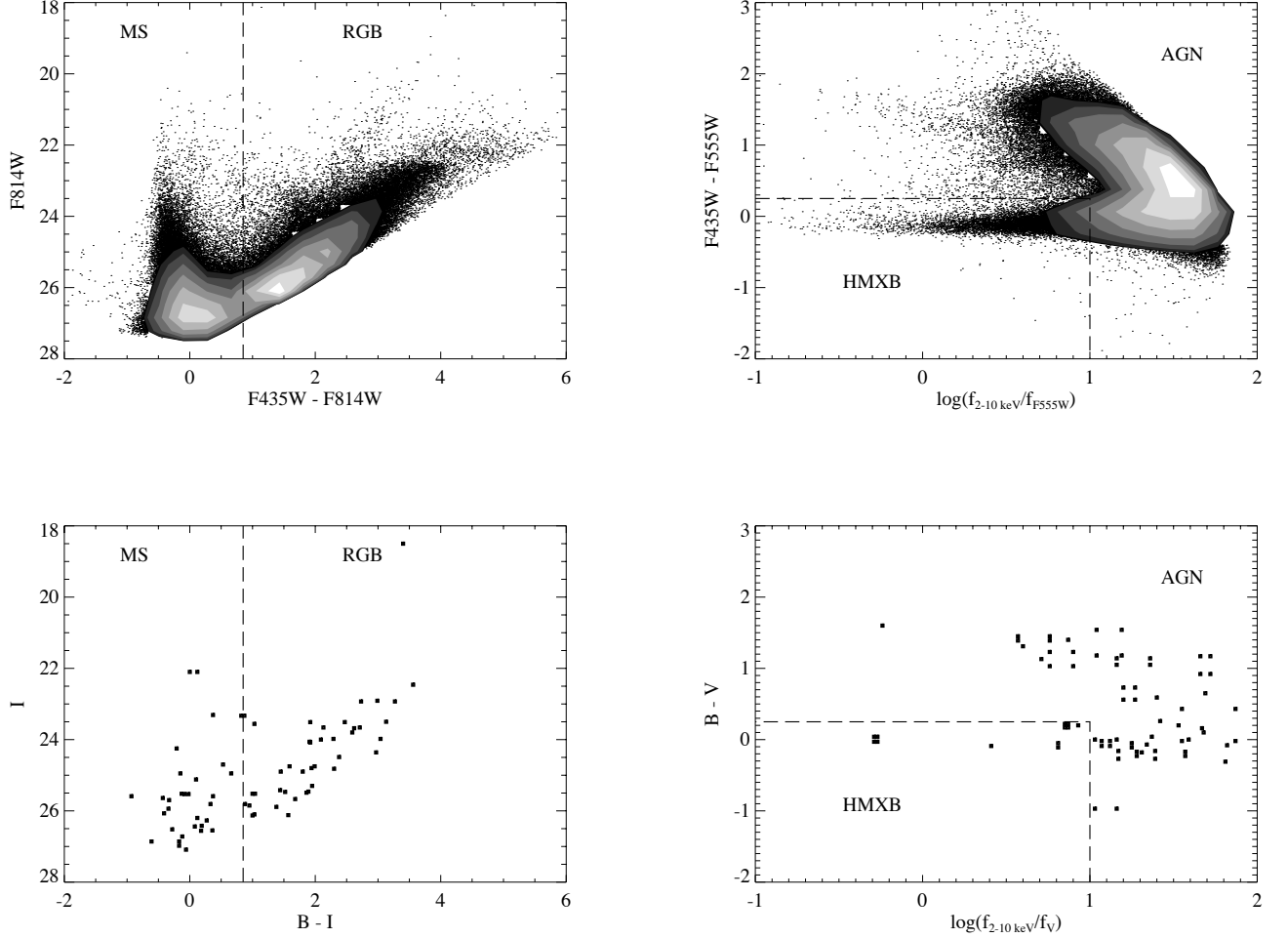


FIG. 8.— Top row: a sample color-magnitude diagram (CMD; left) and X-ray color-magnitude diagram (XCMD; right). The MS and RGB regions are marked on the CMD, and the HMXB and AGN regions are marked on the XCMD. Bottom row: the locations of our candidate optical counterparts as either MS or RGB stars on a CMD (left), and an XCMD (right) showing the actual values of the X-ray/optical flux ratio for our candidate optical counterparts to each X-ray source.

The source classification reported by the `xclass` routine was then compared to the classification determined by our hardness ratio analysis. In some cases, the multiwavelength and hardness ratio classifications disagreed. This was most commonly seen with sources classified as XRBs by our hardness ratio analysis but with multiwavelength properties consistent with a background AGN. In these cases, we favor the AGN classification. Sources that are initially classified as AGN but which exhibit a soft X-ray spectrum (i.e., classified as ‘SOFT’ in our HR analysis) may be potential LMXBs. Only one of our HR-classified SNRs shows X-ray and optical characteristics inconsistent with a SNR origin, and may be an unusually soft background AGN or a foreground star. Our final source classification yields 46 background AGN candidates, 26 HMXB candidates, 11 LMXB candidates, 10 SNRs, and one foreground star. A summary of all X-ray and optical data and our final source classification is present in Table 17.

We use the Cappelluti et al. (2009) AGN  $\log N$ - $\log S$  distribution to estimate the expected number of AGN

in our X-ray source catalog to be  $\sim 50$ . The similarities in both the X-ray and optical properties of AGN and LMXBs (especially at the distance of NGC 300) is likely to cause confusion in separating these two populations. With 47 AGN and 11 LMXB candidates obtained using our source classification scheme, we estimate our X-ray/optical classified  $\log N$ - $\log S$  distribution to differ from the statistical by less than 10%. Our source classification scheme correctly classifies both NGC 300 X-1 (source 80) and SN 2010da (source 73) as HMXBs, which were previously identified as HMXBs in earlier works (see Binder et al. 2011b,a). We are therefore confident that our source classification scheme provides the most reliable indicator of the physical nature of the NGC 300 X-ray sources possible with the available data.

#### 4.3.1. Source 4: Foreground or Background?

As can be seen in Figure 7, X-ray source 4 is coincident with the disk of a background galaxy. This source was not detected by *XMM-Newton*, suggesting a large brightening by a factor of  $\gtrsim 22$ . The source has hardness ratios

TABLE 17  
X-RAY POINT SOURCE CLASSIFICATIONS

Source No.	$r^a$ (kpc)	Location <sup>b</sup> in NGC 300	Variability <sup>c</sup>	In <i>HST</i> footprint?	# Optical Counterparts	Location on CMD	Location on XCMD	Prelim. ID	ID. from HRs	Final ID
(1)	(2)	(3)	(4)	(5)	(6)	(7)	(8)	(9)	(10)	(11)
1	5.2	bkg?	none	no				AGN?	ABS	AGN
2	6.7	bkg?	long	no				AGN	XRb	AGN
3	5.5	bkg?	none	yes	2	RGB	AGN	AGN	SOFT	LMXB?
4	6.7	bkg?	long	yes	1			Galaxy	ABS	Galaxy/FS?
5	4.6	bkg	none	yes	10	MS, RGB	HMXB, AGN	HMXB?	XRb	HMXB

NOTE. — <sup>a</sup>Inclination-corrected galactocentric radius; the X-ray point source population at  $r > 4$  kpc is expected to be dominated by background AGN.

<sup>b</sup>Location in NGC 300 was determined by looking at ground-based *R*-band and  $H\alpha$  imaging. Locations are described as spiral arm, inter-arm regions, or background. X-ray sources that fall beyond the extent of the optical images are labeled as ‘background?’

<sup>c</sup>Variability is classified as ‘long’-term, ‘rapid,’ or ‘none.’

<sup>d</sup>SN 2010da, see Binder et al. (2011b).

<sup>e</sup>NGC 300 X-1, see Binder et al. (2011a).

Only the first five entries are shown.

consistent with those of other XRbS or background AGN. We consider three possible scenarios for the physical nature of source 4: (1) a background, high-redshift quasar, (2) an ultra-luminous X-ray (ULX) source located within the disk of the background galaxy, and (3) a flaring foreground M star.

We first consider the high-redshift quasar interpretation. Source 4 would have a typical quasar X-ray luminosity of  $\sim 10^{45}$  erg s<sup>-1</sup> at a luminosity distance of  $\sim 26$  Gpc, roughly  $z \approx 3$ . However, high-redshift quasars typically exhibit variations in X-ray luminosity on the order of  $\sim 15\%$ , and extreme changes (such as seen in source 4) are rare (Gibson & Brandt 2012).

To evaluate the likelihood of this source being a ULX, we assume the background spiral galaxy has a physical diameter of  $\sim 22$  kpc. We measure the angular diameter of the galaxy to be  $\sim 6''.5$  across, implying the distance to the host galaxy is  $\sim 700$  Mpc. At this distance, source 4 would have a 0.35–8 keV luminosity of  $L_X \sim 7 \times 10^{41}$  erg s<sup>-1</sup>. For a source radiating at the Eddington luminosity, this implies a mass of  $\sim 5000 M_\odot$ . The factor of  $\sim 22$  brightening observed in this source is not typical of ULXs, with the notable exception of HLX-1 in the galaxy ESO 243-49 which has exhibited variations in X-ray luminosity of a factor of  $\sim 20$ –50 (Lasota et al. 2011). The high luminosity of HLX-1 is interpreted as mass accretion via Roche-lobe overflow onto a  $\sim 10^4 M_\odot$  BH. We therefore find the ULX interpretation plausible.

Young, active M dwarfs in the Milky Way undergo X-ray flares, and may provide a natural explanation for the factor of  $\sim 22$  increase in X-ray luminosity exhibited by source 4. Assuming a typical M-dwarf  $\dot{M}_V \sim 10$  and our estimated  $m_V \sim 23.8$  for source 4 implies a distance of  $\sim 60$  pc, yielding an X-ray luminosity of  $\sim 5 \times 10^{27}$  erg s<sup>-1</sup>. The implied X-ray luminosity and color ( $F_{435W} - F_{555W} = 0.9$ ) is typical of a flaring late-type star (typically  $10^{27-29}$  erg s<sup>-1</sup> with  $B - V \sim 0.5 - 1$ , Singh et al. 1999). Using XSPEC, we simulate the spectrum of a stellar corona using the MEKAL model with similar signal-to-noise as source 4 and estimate the hardness ratios produced. We find the hardness ratios of source 4 to be consistent with the predicted hardness ratios, although at low signal-to-noise the spectrum cannot be distinguished from a power law. While we cannot rule out the possibility of an AGN or ULX origin, our obser-

vations are most consistent with being a flaring, late-type star within the Milky Way.

#### 4.4. Comparison to Other X-ray Point Source Populations

It is interesting to compare the properties of the NGC 300 point source population to other galaxies with a range of SFHs, morphologies, and stellar masses ( $M_*$ ). Since HMXBs serve as a tracer of young stellar populations, their numbers should correlate with the recent SFH of their host galaxy (Grimm et al. 2003), while the number of longer-lived LMXBs should correspondingly correlate with the total stellar mass of the host galaxy (Gilfanov 2004). Typically, the ratio  $L_{2-10\text{keV}}/\text{SFR}$  is taken as a measure of the HMXBs in a galaxy, while LMXBs are measured through  $L_{2-10\text{keV}}/M_*$ . Both these ratios are found to correlate with the morphology of the host galaxy (Grimm et al. 2002; Gilfanov 2004).

We estimate the 2–10 keV luminosity for our X-ray/optically classified HMXB candidates to be  $\sim 7 \times 10^{37}$  erg s<sup>-1</sup> and, using equation (22) of Grimm et al. (2003), we derive a predicted SFR for NGC 300 of  $0.12 M_\odot \text{ yr}^{-1}$ . This predicted SFR is in excellent agreement with the average recent SFR of  $0.12 \pm 0.05 M_\odot \text{ yr}^{-1}$  measured by Gogarten et al. (2010). Normalized to the SFR, the HMXBs in NGC 300 emit  $\sim 6 \times 10^{38}$  erg s<sup>-1</sup> ( $M_\odot \text{ yr}^{-1}$ ) in the 2–10 keV band, consistent with the value measured for the Milky Way by Grimm et al. (2002).

We find luminosity of our LMXB candidates normalized to the stellar mass of NGC 300 to be  $\sim 9 \times 10^{27}$  erg s<sup>-1</sup>  $M_\odot^{-1}$ , a factor of  $\sim 5$  lower than is observed in the Milky Way (Grimm et al. 2002). This value of LMXB luminosity normalized by stellar mass is a lower limit, as our source classification scheme is unable to discriminate very well between LMXBs and background AGN. We can provide an upper limit to LMXB luminosity per unit stellar mass by assuming all AGN candidates are actually LMXBs – in this case, the luminosity normalized by the stellar mass of NGC 300 is  $\sim 6.5 \times 10^{28}$  erg s<sup>-1</sup>  $M_\odot^{-1}$ . NGC 300 lacks the prominent nuclear bulge present in the Milky Way (where older LMXBs dominate the X-ray source population), and the gas in NGC 300 (from which new HMXBs could be formed) accounts for  $\sim 26\%$  of the baryonic mass of NGC 300 (Westmeier et al. 2011). Only  $\sim 15\%$  of the baryonic mass of the Milky

Way (Flynn et al. 2006) consists of gas that could potentially form stars. Given the differences in stellar mass, gas content, morphology, and star formation history of NGC 300 and the Milky Way, this observed differences in LMXB populations is not surprising.

When we consider the total XRB population, we find the number of X-ray sources above  $10^{37}$  erg s $^{-1}$  ( $N_X$ ) and the total X-ray luminosity ( $L_X$ , in units of  $10^{38}$  erg s $^{-1}$ ) normalized by the stellar mass (in units of  $10^{11} M_\odot$ ) of NGC 300 to be  $N_X/M_* = 93 \pm 10$  and  $L_X/M_* = 0.47 \pm 0.05$ , respectively. Gilfanov (2004) reported similar ratios of  $L_X/M_*$  for other late-type galaxies, although the average value of  $N_X/M_*$  for the same galaxies was found to be  $\sim 160 \pm 50$ . It should be noted that the comparison between the Gilfanov (2004) sample and NGC 300 comes with two significant caveats: first, the limiting X-ray luminosities of the galaxies examined by Gilfanov (2004) were  $\gtrsim 10^{37}$  erg s $^{-1}$ , and the total number of X-ray sources above  $10^{37}$  erg s $^{-1}$  often had to be estimated; second, the stellar masses of the galaxies sampled were significantly larger than NGC 300 (often by more than an order of magnitude). Therefore, the ratios derived by Gilfanov (2004) may require modifications for deeper X-ray data (below  $\sim 10^{37}$  erg s $^{-1}$ ), and for galaxies with stellar masses comparable to NGC 300.

#### 5. THE $\log N$ - $\log S$ RELATION AND THE X-RAY LUMINOSITY FUNCTION

Numerous studies have shown a correlation between the shape of the XLF of a point source population and the SFH of the host galaxy (Grimm et al. 2003; Eracleous et al. 2006). Those galaxies with a high degree of recent SF have their X-ray emission dominated by young, luminous HMXBs, while older stellar populations show LMXBs as the dominant source of X-ray emission, although this relationship may not be monotonic over a few hundred Myr (Belczynski et al. 2004). Using the *Chandra* X-ray point source catalog and overlapping *HST* exposures, we aim to directly test the XLF slope-age correlation in NGC 300.

The cumulative number of sources above a given flux ( $N(> S)$ , where  $S$  is in units of erg s $^{-1}$  cm $^{-2}$ ) found in a survey covering a total geometric area  $A$  can be evaluated as:

$$N(> S) = \sum_{i, S_i > S} \frac{1}{A(S_i)}. \quad (4)$$

$N(> S)$  has units of sources deg $^{-2}$  and is weighted by the survey area over which each source could have been detected. The  $A(S)$  factor would account for survey completeness if the sources were distributed uniformly, although we do not expect this to be true for sources associated with NGC 300. We terminate the low flux end of the distribution at the 90% limiting luminosity for each energy band considered. The sensitivity maps calculated in Section 2.4 allow the area function  $A(S)$  (the area over which a source with flux  $S$  would be detectable) to be directly evaluated for each source.

We use two approaches to construct the XLF for the NGC 300 point source population. First, we calculate the cumulative  $\log N$ - $\log S$  distributions for the soft (0.5-2 keV) and hard (2-8 keV) bands using all 95 X-ray sources

detected in our *Chandra* observation. Using the background AGN distribution of Cappelluti et al. (2009), we then statistically correct for the anticipated background contamination – we hereafter refer to these XLFs as our “statistical XLFs.”

The statistical XLFs are shown in Figure 9. For each energy band, we model the  $\log N$ - $\log S$  distribution as a power law. For the 0.5-2 keV distribution, we find a best-fit power law index of  $\gamma = 2.03 \pm 0.10$ ; there is a small bend in the XLF at  $\sim 1.6 \times 10^{36}$  erg s $^{-1}$ , although it is not statistically significant. Our 2-8 keV  $\log N$ - $\log S$  distribution power law fit yields an index of  $\gamma = 1.91 \pm 0.05$ .

We next compute the cumulative  $\log N$ - $\log S$  distribution for objects classified as XRBs from our X-ray and optical classification scheme, hereafter referred to as our “X-ray/optically classified XLFs.” We find the  $\log N$ - $\log S$  distributions of our X-ray/optically classified XLFs agree with the statistical XLFs, especially in the 2-8 keV energy range (due to less contamination by soft X-ray emitters such as SNRs). Figure 10 shows the X-ray/optically classified XLFs (red) and our statistical XLFs (black) in both soft and hard bands. Due to their similarity in X-ray spectral shape and optical colors, the mis-classifications are likely to be LMXBs that are incorrectly identified as background AGN (or vice versa), while our HMXB sample is likely to have significantly fewer mis-classifications. The XLFs of X-ray/optically classified AGN are also consistent with the Cappelluti et al. (2009) AGN distribution.

We fit the X-ray/optically classified XLF in both the soft and hard bands with power laws. The 0.5-2 keV XLF has a slope  $\gamma = 2.42 \pm 0.12$ , while the 2-8 keV XLF has  $\gamma = 1.80 \pm 0.07$ . A low-significance kink is observed in the soft XLF, similar to the feature observed in the soft statistical XLF. Our fits are consistent with those derived from the *XMM-Newton* point source catalog of NGC 300 above  $\sim 1.5 \times 10^{36}$  erg s $^{-1}$  (see Carpano et al. 2005, their Figure 5). All the XLF slopes derived here are typical of spiral galaxies with recent star formation activity (Fabbiano 2006; Colbert et al. 2004; Grimm et al. 2003).

To examine whether the bend in the soft XLF near  $3 \times 10^{-15}$  erg s $^{-1}$  cm $^{-2}$  (equivalent to  $\sim 1.6 \times 10^{36}$  erg s $^{-1}$  at the distance of NGC 300) may be due to a specific X-ray population we constructed  $\log N$ - $\log S$  distributions for HMXBs, LMXBs, and SNRs separately. Figure 11 shows the soft  $\log N$ - $\log S$  distributions for each of these three groups, as well as the statistical XLF. We find that the HMXBs (black line) are the only population without a significant number of sources at fainter luminosities. It is possible that there exists a substantial population of lower luminosity, wind-fed HMXBs that would require deeper observations to detect at high significance. Alternatively, the change in the XLF slope may be due to XRTs that are observable only during their more luminous outbursting phase (and fall below our detection threshold during quiescence). Table 18 summarizes our best-fit power law slopes for each of our XLFs.

##### 5.1. Radial $\log N$ - $\log S$ Distributions

We next searched for radial trends in our NGC 300 X-ray source population. We divided our X-ray/optically classified XRB candidates into two radial bins: an “in-

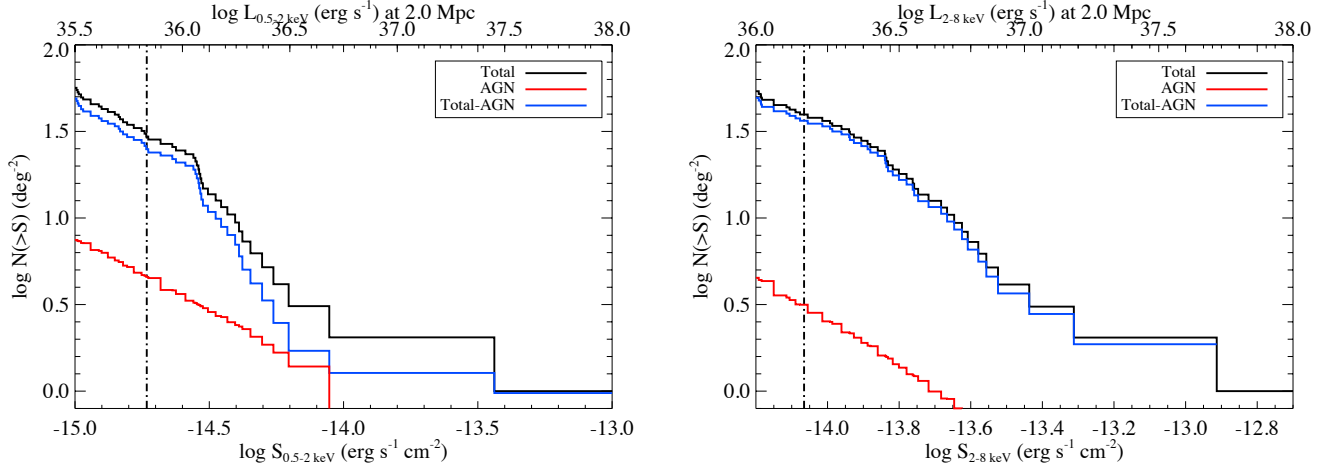


FIG. 9.— The cumulative 0.5-2 keV (left) and 2-8 keV (right) X-ray  $\log N$ - $\log S$  distributions for the NGC 300 X-ray sources. The dot-dashed lines indicate the 90% limiting flux for our survey in each band. The AGN  $\log N$ - $\log S$  model from Cappelluti et al. (2009) was assumed (red). The AGN-subtracted  $\log N$ - $\log S$  distribution is shown in blue.

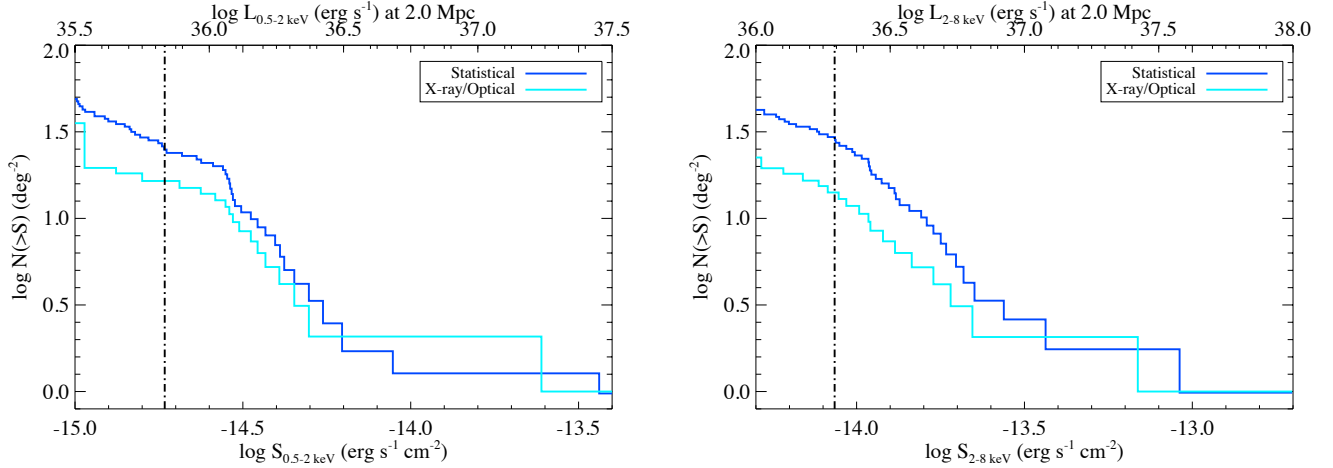


FIG. 10.— The 0.5-2 keV (left) and 2-8 keV (right)  $\log N$ - $\log S$  distributions for our background-subtracted total  $\log N$ - $\log S$  distributions (blue) and our X-ray/optically classified XRB candidates (cyan).

TABLE 18  
POWER LAW FITS TO THE NGC 300  $\log N$ - $\log S$  DISTRIBUTIONS

$\log N$ - $\log S$ Distribution	0.5-2 keV	2-8 keV
Statistically XLF	$2.03 \pm 0.10$	$1.91 \pm 0.05$
X-ray/optically Classified XLF	$2.42 \pm 0.12$	$1.80 \pm 0.07$
X-ray/optical XLF, $r < 2.7$ kpc	$1.68 \pm 0.31$	$1.63 \pm 0.18$
X-ray/optical XLF, $2.7 < r < 5.4$ kpc	$2.65 \pm 0.55$	$1.23 \pm 0.07$
HMXBs	$1.86 \pm 0.19$	$1.56 \pm 0.09$
LMXBs	$2.73 \pm 0.30$	$1.69 \pm 0.29$
SNRs	$1.04 \pm 0.01$	N/A

ner” region ( $d < 2.7$  kpc) and “outer” region (2.7-5.4 kpc) so that we could directly compare our  $\log N$ - $\log S$  distributions to the radial SFHs measured by Gogarten et al. (2010). Using the SFHs at different epochs (Gogarten et al. 2010), we assign an approximate, weighted average age to each radial bin. The radial  $\log N$ - $\log S$  distributions in both the soft and hard bands are shown in Figure 12.

We observe a preliminary correlation towards flatter 2-8 keV XLF slope with increasing galactocentric radius and younger average age of the underlying stellar population. This trend is not observed in the soft band, which may suffer more severely from contamination from SNRs or foreground stars or from obscuration. We therefore consider the 2-8 keV XLF a more reliable diagnostic of the XRB population. In Figure 13, we compare our ra-

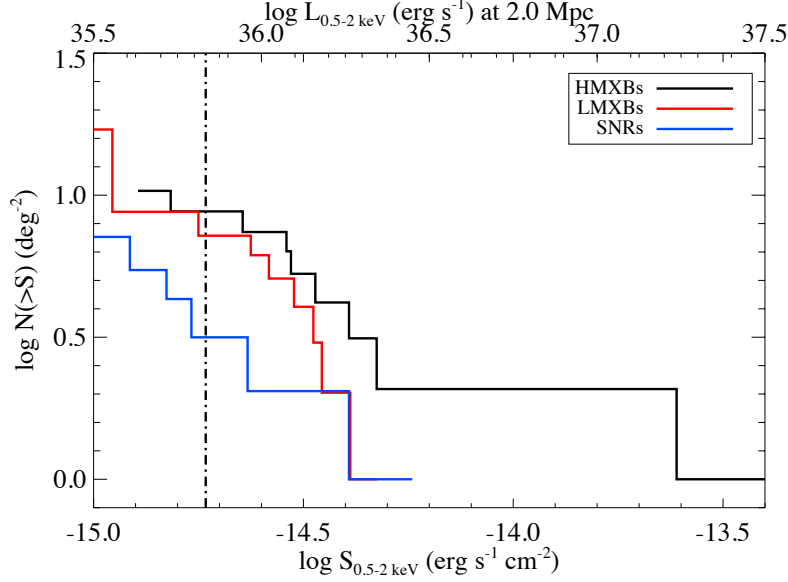


FIG. 11.— The 0.5-2 keV  $\log N$ - $\log S$  distribution for HMXBs (solid black), LMXBs (red), and SNRs (blue) as classified based on our X-ray and optical observations. The dashed line shows the statistical XRB  $\log N$ - $\log S$  using the Cappelluti et al. (2009) background AGN distribution. We find HMXBs are the only sub-group without a significant number of sources detected at fainter luminosities, potentially producing the break near  $3 \times 10^{-15}$  erg s $^{-1}$  cm $^{-2}$ .

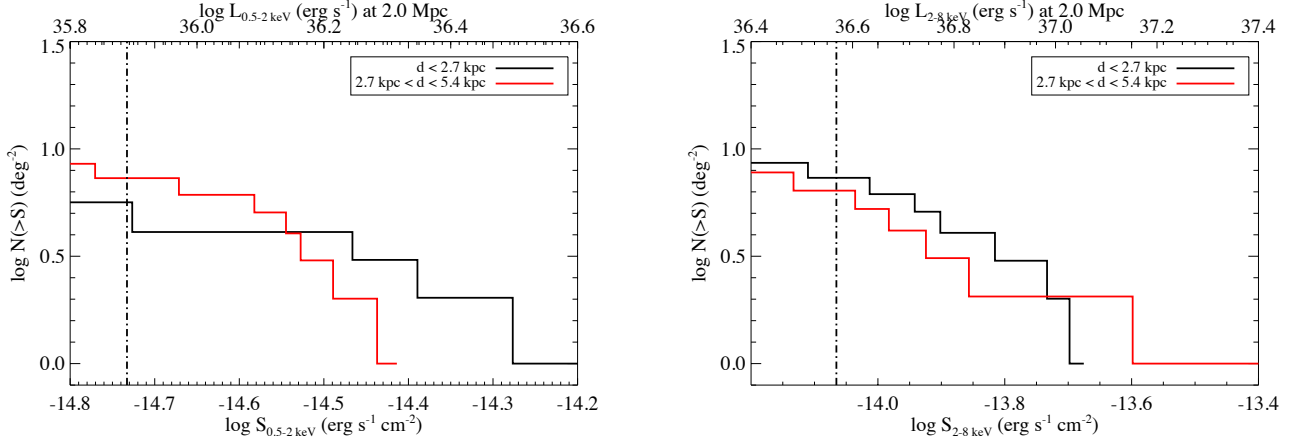


FIG. 12.— The 0.5-2 keV (left) and 2-8 keV (right)  $\log N$ - $\log S$  distributions for X-ray/optically identified XRBs detected within the inner 2.7 kpc (black) and outer 2.7-5.4 kpc (red) regions.

dial XLF/age data to model predictions (Eracleous et al. 2006). X-ray sources detected at smaller galactocentric radii ( $< 2.7$  kpc) show an average older age,  $\sim 83$  Myr, and a steeper XLF slope ( $\gamma \sim 1.6$ ) than those sources found in the outer regions of the NGC 300 disk (59 Myr in age with  $\gamma \sim 1.2$ ).

Our X-ray/optical data of NGC 300 thus constitutes one of the first tests of such model predictions relating the nature of the X-ray sources to the underlying stellar population of a galaxy; additional XLF-SFH measurements will become available when the remaining four CLVS galaxies (NGC 404, NGC 55, NGC 2403, and NGC 4214) are analyzed in upcoming works.

## 6. SUMMARY AND CONCLUSIONS

We have presented the X-ray point source catalog for a new, deep *Chandra* observation of NGC 300 as part of the *Chandra* Local Volume Survey. A total of 95 sources were detected in NGC 300 down to a 90% limiting 0.35-8 keV luminosity of  $\sim 1.5 \times 10^{36}$  erg s $^{-1}$ . By comparing our X-ray source catalog to earlier observations of NGC 300 performed by *XMM-Newton*, we were able to place long-term variability constraints on each source and identify 25 XRT candidates. We fit the radial X-ray source distribution to an exponential profile and were able to derive a scale length of  $1.7 \pm 0.2$  kpc, in good agreement with measurements taken at other wavelengths. We evaluated hardness ratios for each of our X-ray sources, and performed spectral fitting for those sources with more than 50 counts.

We utilized nine deep *Hubble Space Telescope* fields



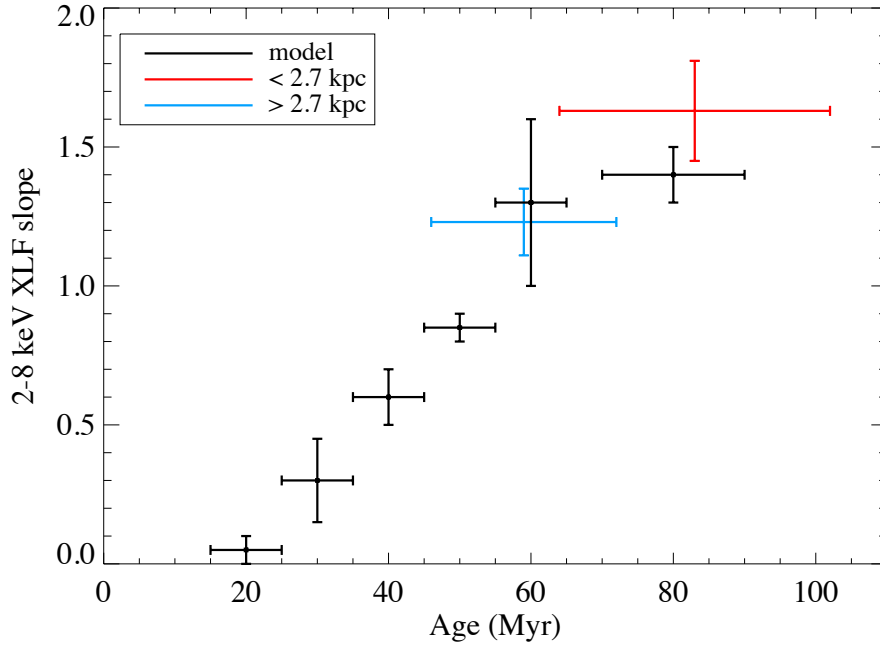


FIG. 13.— The slope of the cumulative 2-8 keV XLF as a function of stellar age. Black points indicate model predictions. The red cross indicates our data for radial bins less than 2.7 kpc, while the blue cross shows our data for X-ray sources from 2.7 - 5.4 kpc. Our combined *Chandra/HST* data of NGC 300 agree very well with predictions, and further analysis of the remaining CLV galaxies will provide further tests of these model predictions.

to search for optical counterparts to each of our X-ray sources; 32 of our X-ray sources were observed in at least one of the overlapping *HST* fields. We developed a new source classification method which combined both X-ray and optical data to classify each source as a HMXB, LMXB, or background AGN, and have made our IDL routine which automates our source classification technique publicly available. We classified 47 sources as background AGN, 26 as HMXBs, 11 as LMXBs, 10 as SNRs, and one as a foreground star.

The cumulative  $\log N$ - $\log S$  distributions were presented in both 0.5-2 and 2-8 keV bands and found to be consistent with those of other spiral galaxies with a dominant HMXB population. Additionally, we divided our X-ray sources into two radial bins and modeled the radially-resolved  $\log N$ - $\log S$  distributions with power laws. Using the SFHs of Gogarten et al. (2010), we were able to assign an average to the underlying stellar populations, and we find the measured XLF slopes and stellar population

ages to be in good agreement with model predictions. The remaining four CLVS galaxies (NGC 55, NGC 404, NGC 2403, and NGC 4214) will provide additional constraints on XLF-age models with upcoming works.

Support for this work was provided by the National Aeronautics and Space Administration through Chandra Award Number G01-12118X issued by the Chandra X-ray Observatory Center, which is operated by the Smithsonian Astrophysical Observatory for and on behalf of the National Aeronautics Space Administration under contract NAS8-03060. T.J.G and P.P.P acknowledge support under NASA contract NAS8-03060. This research has made use of the NASA/IPAC Extragalactic Database (NED) which is operated by the Jet Propulsion Laboratory, California Institute of Technology, under contract with the National Aeronautics and Space Administration.

## REFERENCES

08. 1  
 Belczynski, K., Kalogera, V., Zezas, A., & Fabbiano, G. 2004, *ApJ*, 601, L147  
 Binder, B., Williams, B. F., Eracleous, M., Garcia, M. R., Anderson, S. F., & Gaetz, T. J. 2011a, *ApJ*, 742, 128  
 Binder, B., et al. 2011b, *ArXiv e-prints*  
 Blair, W. P., & Long, K. S. 1997, *ApJS*, 108, 261  
 Broos, P. S., Townsley, L. K., Feigelson, E. D., Getman, K. V., Bauer, F. E., & Garmire, G. P. 2010, *ApJ*, 714, 1582  
 Cappelluti, N., et al. 2009, *A&A*, 497, 635  
 Carpano, S., Wilms, J., Schirmer, M., & Kendziorra, E. 2005, *A&A*, 443, 103  
 Colbert, E. J. M., Heckman, T. M., Ptak, A. F., Strickland, D. K., & Weaver, K. A. 2004, *ApJ*, 602, 231  
 Corbelli, E., & Salucci, P. 2000, *MNRAS*, 311, 441  
 Dalcanton, J. J., et al. 2009, *ApJS*, 183, 67  
 Deharveng, L., Caplan, J., Lequeux, J., Azzopardi, M., Breysacher, J., Tarengi, M., & Westerlund, B. 1988, *A&AS*, 73, 407  
 Eracleous, M., Sipior, M. S., & Sigurdsson, S. 2006, in *IAU Symposium*, Vol. 230, *Populations of High Energy Sources in Galaxies*, ed. E. J. A. Meurs & G. Fabbiano, 417  
 Fabbiano, G. 2006, *ARA&A*, 44, 323  
 Flynn, C., Holmberg, J., Portinari, L., Fuchs, B., & Jahreiß, H. 2006, *MNRAS*, 372, 1149  
 Ford, H. C., et al. 1998, in *Society of Photo-Optical Instrumentation Engineers (SPIE) Conference Series*, Vol. 3356, *Society of Photo-Optical Instrumentation Engineers (SPIE) Conference Series*, ed. P. Y. Bely & J. B. Breckinridge, 234  
 Freedman, W. L., & Madore, B. F. 1988, *ApJ*, 332, L63



- Freeman, P. E., Kashyap, V., Rosner, R., & Lamb, D. Q. 2002, *ApJS*, 138, 185
- Gehrels, N. 1986, *ApJ*, 303, 336
- Georgakakis, A., Nandra, K., Laird, E. S., Aird, J., & Trichas, M. 2008, *MNRAS*, 388, 1205
- Gibson, R. R., & Brandt, W. N. 2012, *ApJ*, 746, 54
- Gilfanov, M. 2004, *MNRAS*, 349, 146
- Gogarten, S. M., et al. 2010, *ApJ*, 712, 858
- Grimm, H.-J., Gilfanov, M., & Sunyaev, R. 2002, *A&A*, 391, 923
- Grimm, H.-J., Gilfanov, M., & Sunyaev, R. 2003, *MNRAS*, 339, 793
- Hornschemeier, A. E., et al. 2001, *ApJ*, 554, 742
- Kalberla, P. M. W., Burton, W. B., Hartmann, D., Arnal, E. M., Bajaja, E., Morras, R., & Pöppel, W. G. L. 2005, *A&A*, 440, 775
- Kilgard, R. E., et al. 2005, *ApJS*, 159, 214
- Kim, S. C., Sung, H., Park, H. S., & Sung, E.-C. 2004, *Chin. J. Astron. Astrophys.*, 4, 299
- Kong, A. K. H., & Di Stefano, R. 2003, *ApJ*, 590, L13
- Kong, A. K. H., Garcia, M. R., Primini, F. A., Murray, S. S., Di Stefano, R., & McClintock, J. E. 2002, *ApJ*, 577, 738
- Larsen, S. S., & Richtler, T. 2000, *A&A*, 354, 836
- Lasota, J.-P., Alexander, T., Dubus, G., Barret, D., Farrell, S. A., Gehrels, N., Godet, O., & Webb, N. A. 2011, *ApJ*, 735, 89
- Long, K. S., et al. 2010, *ApJS*, 187, 495
- Maíz-Apellániz, J., Cieza, L., & MacKenty, J. W. 2002, *AJ*, 123, 1307
- McGowan, K. E., et al. 2008, *MNRAS*, 383, 330
- McMillan, P. J. 2011, *MNRAS*, 414, 2446
- Muñoz-Mateos, J. C., Gil de Paz, A., Boissier, S., Zamorano, J., Jarrett, T., Gallejo, J., & Madore, B. F. 2007, *ApJ*, 658, 1006
- Nandra, K., et al. 2005, *MNRAS*, 356, 568
- Pannuti, T. G., Duric, N., Lacey, C. K., Goss, W. M., Hoopes, C. G., Walterbos, R. A. M., & Magnor, M. A. 2000, *ApJ*, 544, 780
- Park, T., Kashyap, V. L., Siemiginowska, A., van Dyk, D. A., Zezas, A., Heinke, C., & Wargelin, B. J. 2006, *ApJ*, 652, 610
- Plucinsky, P. P., et al. 2008, *ApJS*, 174, 366
- Prestwich, A. H., Kilgard, R. E., Primini, F., McDowell, J. C., & Zezas, A. 2009, *ApJ*, 705, 1632
- Puche, D., Carignan, C., & Bosma, A. 1990, *AJ*, 100, 1468
- Read, A. M., & Pietsch, W. 2001, *A&A*, 373, 473
- Shtykovskiy, P., & Gilfanov, M. 2005, *MNRAS*, 362, 879
- Shtykovskiy, P. E., & Gilfanov, M. R. 2007, *Astronomy Letters*, 33, 437
- Singh, K. P., Drake, S. A., Gotthelf, E. V., & White, N. E. 1999, *ApJ*, 512, 874
- Skrutskie, M. F., et al. 2006, *AJ*, 131, 1163
- Smith, R. K., Brickhouse, N. S., Liedahl, D. A., & Raymond, J. C. 2001, *ApJ*, 556, L91
- Soria, R., & Kong, A. K. H. 2002, *ApJ*, 572, L33
- Tikhonov, N. A., Galazutdinova, O. A., & Drozdovsky, I. O. 2005, *A&A*, 431, 127
- Trudolyubov, S. P., Borozdin, K. N., Priedhorsky, W. C., Mason, K. O., & Cordova, F. A. 2002, *ApJ*, 571, L17
- Tüllmann, R., et al. 2011, *ApJS*, 193, 31
- Vila-Costas, M. B., & Edmunds, M. G. 1992, *MNRAS*, 259, 121
- Westmeier, T., Braun, R., & Koribalski, B. S. 2011, *MNRAS*, 410, 2217
- Williams, B. F., Dalcanton, J. J., Dolphin, A. E., Holtzman, J., & Sarajedini, A. 2009, *ApJ*, 695, L15
- Williams, B. F., et al. 2008, *ApJ*, 680, 1120
- Wilms, J., Allen, A., & McCray, R. 2000, *ApJ*, 542, 914
- Yi, I., & Boughn, S. P. 1998, *ApJ*, 499, 198